



1 Restratification at a California Current Upwelling Front, Part 2: Dynamics

2 Leah Johnson*

3 *Brown University, Providence, RI*

4 Craig M. Lee

5 *Applied Physics Laboratory, Seattle, WA*

6 Eric A. D'Asaro

7 *Applied Physics Laboratory, Seattle, WA*

8 Jacob O. Wenegrat

9 *Stanford University, Stanford, CA*

10 Leif N. Thomas

11 *Stanford University, Stanford, CA*

12 *Corresponding author address: Department of Earth, Environmental and Planetary Sciences,

13 Brown University, Providence, RI

14 E-mail: leah.johnson@brown.edu

ABSTRACT

15 A coordinated multi-platform campaign collected detailed measurements of
16 a restratifying surface intensified upwelling front within the California Cur-
17 rent System. A previous manuscript outlined the evolution of the front, re-
18 vealing the importance of lateral advection at tilting isopycnals and increasing
19 stratification in the surface boundary layer with a buoyancy flux equivalent to
20 2000 W m^{-2} . Here, observations were compared with idealized models to
21 explore the dynamics contributing to the stratification. A 2-D model com-
22 bined with a reduced form of the horizontal momentum equations highlight
23 the importance of transient Ekman dynamics, turbulence and thermal wind
24 imbalance at modulating shear in the boundary layer. Specifically, unsteady
25 frictional adjustment to the rapid decrease in wind stress created vertically
26 sheared currents that advected horizontal gradients to increase vertical strati-
27 fication on superinertial timescales. The magnitude of stratification depended
28 on the strength of the horizontal buoyancy gradient. This enhanced strati-
29 fication due to horizontal advection inhibited night-time mixing that would
30 have otherwise eroded stratification from the diurnal warm layer. This un-
31 derscores the importance of near surface lateral restratification for the upper
32 ocean buoyancy budget on diel timescales.

33 **1. Introduction**

34 In regions with strong lateral density contrasts, density fronts can slump, transforming horizontal
35 buoyancy gradients into vertical stratification on timescales that compete with surface forcing
36 variability. The surface ocean is populated with fronts ranging in size from mesoscale $O(10 - 100$
37 km) to submesoscale $O(0.1 - 10$ km) (Rudnick 1999; Hosegood et al. 2006; Mahadevan et al.
38 2012; Thompson et al. 2016), which have cumulative impacts on basin scale stratification, surface
39 potential vorticity (PV) and the distribution of heat, salt, and biogeochemical tracers within the
40 upper ocean (Su et al. 2018; Lévy et al. 2010; Fox-Kemper et al. 2011; Wenegrat et al. 2018).

41 A global analysis suggests that frontal processes are responsible for enhanced stratification in
42 the upper oceans during the transition into spring (Johnson et al. 2016) and direct observations of
43 frontal slumping reveal the importance of horizontal gradients on the upper ocean buoyancy budget
44 in different regions (e.g. North Pacific, Hosegood et al. (2006); Arctic, Timmermans and Winsor
45 (2013); and Oregon Coast, Dale et al. (2008)). Yet the dominant dynamical processes responsible
46 for the rearrangement of buoyancy at fronts remains elusive as interpreting direct observations of
47 frontal slumping are challenging due to the time-space aliasing inherent in surveying such rapidly
48 evolving features. Observations that can help elucidate the dynamics leading to stratification at
49 upper ocean fronts are essential for identifying the role of horizontal buoyancy gradients on the
50 momentum and buoyancy budget of the upper ocean.

51 A set of observations reported in a previous manuscript (Part 1: Observations, hereafter CCF1)
52 described a Lagrangian view of a stratifying submesoscale front in the California Current System.
53 The frontal evolution was divided into three stages: Stage 1, downfront winds and turbulent mix-
54 ing in the boundary layer, BL. Stage 2, diurnal warming and frontal slumping. Stage 3, night-time
55 surface cooling and winds, rapid near surface stratification. This manuscript aims to describe the

56 dynamics responsible for the rapid restratification by incorporating numerical models alongside
 57 the observational analysis described in CCF1. Analyses in CCF1 showed that the observed strati-
 58 fication was due to lateral advection of the cross-frontal gradients by vertically sheared horizontal
 59 currents. The main focus of the modelling here is to understand the dynamics of these currents.

60 The hydrostatic equation for horizontal momentum can be written

$$\frac{D\mathbf{u}_h}{Dt} = -f\hat{\mathbf{z}} \times \mathbf{u}_h - \frac{1}{\rho_o} \nabla p + \frac{\partial}{\partial z} \left(v \frac{\partial \mathbf{u}_h}{\partial z} \right) \quad (1)$$

61 where f is the Coriolis parameter, v is the turbulent eddy viscosity associated with the boundary
 62 layer, and p the reduced pressure.

63 The vertical derivative of (1) was adopted to focus on vertical shear, yielding

$$\frac{\partial}{\partial t} \frac{\partial u}{\partial z} = f \frac{\partial v}{\partial z} - \frac{\partial b}{\partial x} + \frac{\partial^2}{\partial z^2} \left(v \frac{\partial u}{\partial z} \right) \quad (2)$$

$$\frac{\partial}{\partial t} \frac{\partial v}{\partial z} = -f \frac{\partial u}{\partial z} - \frac{\partial b}{\partial y} + \frac{\partial^2}{\partial z^2} \left(v \frac{\partial v}{\partial z} \right) \quad (3)$$

64 where the advective terms were ignored and the pressure term was replaced with density us-
 65 ing the hydrostatic approximation $\partial p / \partial z = -g\rho$ and buoyancy $b = -g\rho/\rho_o$. This system of
 66 equations was combined into one in complex form assuming $Y = \partial u / \partial z + i\partial v / \partial z$ and $M^2 =$
 67 $\partial b / \partial x + i\partial b / \partial y$:

$$\frac{\partial}{\partial t} Y = -ifY - M^2 + \frac{\partial^2}{\partial z^2} (vY) \quad (4)$$

(TEND) (CORI) (PRES) (DIFF)

68 describing the shear tendency (TEND) resulting from the inertial term (CORI), the pressure gra-
 69 dient (PRES) and friction (DIFF). The boundary conditions were
 70

$$vY = \frac{1}{\rho} T \quad \text{at } z = 0, \quad vY = 0 \quad \text{at } z = -H. \quad (5)$$

71 where H is the mixed layer depth and $T = \tau^x + i\tau^y$ is the complex wind stress at the surface.

72 Note the combination of balances encapsulated in (4): TEND and CORI capture internal waves
73 with frequency set at the earth's rotation. The evolution of TEND, CORI, and PRES were ex-
74 plored by Tandon and Garrett (1994) (TG94) in an inviscid frontal adjustment of nearly vertical
75 isopycnals at rest. TEND, CORI, and DIFF is the time dependent Ekman problem (McWilliams
76 and Huckle 2006; Wenegrat and McPhaden 2016) and when integrated vertically becomes the slab
77 ML model of wind driven near inertial oscillations (NIO, Pollard and Millard (1970)). CORI and
78 PRES, is thermal wind balance, and adding DIFF becomes turbulent thermal wind (TTW, Gula
79 et al. (2014); McWilliams et al. (2015)), also known as the generalized Ekman model (Cronin
80 and Kessler 2009; Wenegrat and McPhaden 2016). It will be shown that each of these balances
81 alone are insufficient to describe the observations, yet when combined, work to create a shear ten-
82 dency capable of tilting isopycnals and enhancing stratification comparable with the observations
83 in CCF1.

84 Dauhajre and McWilliams (2018) employed a framework similar to (4) to investigate the diurnal
85 cycle on a wind forced front. The results suggested a transition between two phases. Night-time
86 winds and cooling induced turbulent mixing and an overturning circulation as the front approached
87 TTW balance. The onset of solar warming decreased turbulent fluxes, leaving a front out of
88 thermal wind balance and in an unsteady state. This state resulted in an inertial response of the
89 front akin to low level jets developed in the atmosphere (Van de Wiel et al. 2010). The system
90 transitioned back towards a diffusive regime with the onset of night-time cooling that damped
91 the inertial oscillation and redeveloped a TTW circulation. Dauhajre and McWilliams (2018)
92 explored the rectification of time dependence on classical TTW as a modified transient turbulent
93 thermal wind (T3W). The observations in CCF1 describe a slightly different regime than the T3W
94 problem in that there was a rapid decrease in convective and wind driven turbulence as opposed
95 to steady wind forcing. The implied response of the front to this rapid decrease in wind-driven

⁹⁶ mixing was an adjustment from a state of thermal wind imbalance set by nearly vertical isopycnals,
⁹⁷ ageostrophic shear and momentum flux divergence.

⁹⁸ In section 3, a one dimensional model (1D) is used to show that the rapid appearance of stratifi-
⁹⁹ cation cannot be simulated by vertical mixing physics alone. In section 4, a two-dimensional (2D)
¹⁰⁰ model including turbulence viscosity and driven by the observed forcing heat flux and wind stress
¹⁰¹ is used to simulate the response of the ocean. Due to the lack of frontogenesis in this model, the
¹⁰² lateral gradients were an order of magnitude less than observed in CCF1. Nevertheless, the 2D
¹⁰³ results can be accurately reproduced by solving (4) using the average turbulent viscosity (1D+),
¹⁰⁴ as shown in section 4a. Furthermore, when non-dimensionalized by balanced Richardson number
¹⁰⁵ (Ri_b), 2D and 1D+ are shown to reproduce the observed increase in stratification (section 4b),
¹⁰⁶ signifying that the observed currents, and thus the restratification, is controlled by dynamics in the
¹⁰⁷ reduced set of equations (4). Finally, the observations (OBS) contrasted with 1D, 2D and 1D+
¹⁰⁸ provide insight into the role of along-front variability present in the observations as described in
¹⁰⁹ CCF1.

¹¹⁰ 2. Model Set-up and Observations

¹¹¹ The models employed here include Price–Weller–Pinkel (Price et al. (1986); hereafter 1D), the
¹¹² MITgcm (Marshall et al. (1997); hereafter 2D), and the reduced set of equations (4; hereafter 1D+).
¹¹³ The models were forced and initialized with the observations. A hyperbolic tangent function was
¹¹⁴ used to approximate the observed cross frontal structure of T and S that sets the initial conditions
¹¹⁵ for the models (see Appendix).

¹¹⁶ a. 1D Set-up

¹¹⁷ The 1-D upper ocean response to the observed surface forcing was explored using the
¹¹⁸ Price–Weller–Pinkel model (Price et al. (1986); 1D), similar to that implemented in Farrar et al.
¹¹⁹ (2007). The approximated cross frontal structure (see Appendix) was horizontally averaged to
¹²⁰ produce a single initial profile of T and S . The model was run with 1 m vertical resolution and a
¹²¹ 60 s time-step. The time span began at the onset of winds (yd 210, 6 days before the start of the
¹²² survey), and the model was run for 8 days (when the survey ended).

¹²³ b. 2D Set-up

¹²⁴ The MITgcm (2D) was run in hydrostatic mode with a grid resolution of 300 m in the horizontal
¹²⁵ and 3 m in the vertical. The domain was horizontally periodic, with two fronts approximately 95
¹²⁶ km apart. The configuration included 2 grid cells in the along front direction, for a total of 600 m.
¹²⁷ Details of the model set-up can be found in the Appendix. Changes in the along front direction
¹²⁸ are negligible and therefore the model is considered 2-D. The vertical extent was 0 to 150 m in
¹²⁹ depth. In this 2D configuration, northerly winds were exactly downfront and did not account
¹³⁰ for the curvature of the front, which modified the orientation between wind stress and horizontal
¹³¹ buoyancy gradient compared to OBS. Results are presented in terms of along front (u^{af} , positive
¹³² south in OBS) and cross front (u^{xf} positive east in OBS). The model began with the onset of
¹³³ winds (yd 210, 6 days before the survey) which allowed for a comprehensive study of unsteady
¹³⁴ wind forcing on the front.

¹³⁵ c. 1D+ Set-up

¹³⁶ A reduced model (1D+) was evaluated by solving (4) numerically. The vertical derivatives were
¹³⁷ solved using a second order finite difference discretization operator and then stepped forward

¹³⁸ with a Crank-Nicolson method, an implicit method for solving stiff ordinary differential equations
¹³⁹ (ODEs) (LeVeque 2007). Boundary conditions (5) were included in the discretized operator in
¹⁴⁰ DIFF. The 1D+ model was solved at every grid point across the front in 2D, initialized with a
¹⁴¹ profile of Y , v , and M^2 from 2D at the time the observed float gets trapped near the surface (y_d
¹⁴² 216.3, stage 2). Profiles of v and M^2 were set constant in time and the solution was integrated
¹⁴³ in z to obtain values for u^{af} and u^{xf} assuming no motion at the bottom. Solutions here were
¹⁴⁴ considered 1-D as they were decoupled from neighboring grid points and therefore do not include
¹⁴⁵ frontogenesis or advection of momentum.

¹⁴⁶ *d. Observations*

¹⁴⁷ Model results were compared with a coordinated set of observations using a Lagrangian float
¹⁴⁸ and a ship-towed Triaxus profiling vehicle (details in CCF1). The observed and simulated front
¹⁴⁹ was surface intensified above a pycnocline at \sim 30 m. This near surface layer will be referred to
¹⁵⁰ as the mixed layer (ML) for simplicity, though, consistent with many other studies, this layer was
¹⁵¹ not always well mixed in momentum and buoyancy. A comparison between 1D, 2D and OBS is
¹⁵² seen in Fig. 1.

¹⁵³ **3. 1D: Surface Buoyancy and Momentum**

¹⁵⁴ In the absence of horizontal stratification, the upper ocean buoyancy budget responds to mo-
¹⁵⁵ mentum and buoyancy fluxes at the surface. The observations spanned 30 hr, capturing a cycle of
¹⁵⁶ night-time mixing that bracketed day-time warming. This diurnal forcing imprinted buoyancy and
¹⁵⁷ momentum in the near surface layers. Although the model was initiated 6 days prior to the survey,
¹⁵⁸ only results coinciding with the observations are discussed here.

159 In 1D, the onset of day-time warming along with decreased winds (stage 2) shoaled the once
160 well mixed layer that persisted for several days of strong winds (i.e., prior and during stage 1).
161 During stage 2, the near surface layer warmed, building stratification in the upper 3 m. The onset
162 of winds and night-time cooling (stage 3) simultaneously eroded the diurnal stratification and
163 pushed it deeper into the water column, much like other models of the diurnal cycle (Price et al.
164 1986). At this time, the distribution of stratification in OBS deviated from the simple model (Fig.
165 1), as it increased throughout the ML (e.g. at 15 m, below the 1D ML) and was enhanced near the
166 surface.

167 The difference in vertical gradients of T , S , and ρ from OBS and 1D highlight the importance
168 of horizontal and vertical variability. During diurnal warming, the float was trapped at 2 m and
169 therefore provided information near the surface (Fig. 2). In this near surface layer, the float
170 captured diurnal changes in N^2 and T_z similar to 1D. Yet, increases in S_z observed by the float in the
171 absence of freshwater forcing suggests horizontal advection not captured by the 1-D simulation.
172 Additionally, Triaxus measured stratification deeper in the ML that was completely absent in 1D.
173 This is evidence of warm fresh water sliding over the cold salty upwelled waters defining the front.
174 The largest difference between 1D and OBS occurred at the onset of stage 3 as surface cooling and
175 increased winds (yd 216.8) eroded the day-time stratification in 1D. In OBS, the near surface layer
176 continued to stratify, resisting the tendency of surface forcing to erode near surface stratification.
177 This difference between 1D and OBS, with the large observed gradients in T and S , reveal the
178 importance of lateral stratification on the upper ocean buoyancy budget.

179 While 1D had some skill at capturing a thin diurnal warm layer observed by the float, it failed
180 to capture the evolution of stratification deeper in the ML as well as the enhanced stratification
181 during stage 3. In these cases, the salinity structure in the absence of freshwater forcing brings
182 attention to key role of horizontal advection. The rest of this study considers lateral processes.

183 **4. 2D: Friction, Inertial Motions, Turbulent Mixing**

184 *a. Adjustment and turbulence*

185 The transient response of the front to unsteady winds in 2D is apparent in (Fig. 3), as Ekman
186 transport from downfront winds advected the front towards the warm (less dense) side of the front.

187 As the winds subsided, both the modeled front and the observed front curved back towards the
188 cold (dense) side of the front, and the modeled front continued to oscillate.

189 The oscillations in 2D can be described by an inertial response to wind forcing averaged through-
190 out the ML (Pollard and Millard 1970):

$$\frac{du}{dt} - fv = \frac{\tau_x}{\rho_o H} \quad (6)$$

191

$$\frac{dv}{dt} + fu = \frac{\tau_y}{\rho_o H}. \quad (7)$$

192 Equations (6) and (7) were solved for the entire length of the model runs initialized when $\tau \approx 0$
193 assuming $u_i^{af} = u_i^{xf} = 0$, and $H = 30$ m (Fig. 3 c-e). The solutions to (6) and (7) agree well
194 with 1D and 2D, suggesting the wavelike pattern after the winds subsided were wind driven near
195 inertial oscillations (NIO). Similarly, in the observations, the float slowed (Fig. 3 e) and turned
196 eastwards (Fig. 3 b, c), albeit at a pace faster than the 2D model. The observations also exhibited
197 higher frequency oscillations not captured by NIO, suggesting along front variability associated
198 with either physical meanders or superinertial motions along the front.

199 The persistent winds diffused the front in 2D causing a weaker horizontal buoyancy gradient than
200 observed (Fig. 4). The difference can be attributed to a lack of external strain in 2D compared
201 to OBS (CCF1). Nonetheless, the agreement between OBS and 2D as wind forcing decreased
202 suggests an inertial response of the front. Though (6) and (7) are appropriate for a slab ML,

203 they cannot capture the shear within the ML responsible for tilting isopycnals and increasing
204 stratification as in OBS.

205 Equation (4) suggests that the evolution of shear will depend on the imbalance of the inertial
206 terms (CORI + PRES), and friction (DIFF). These terms were evaluated in 2D using the time-
207 integrated vertical derivatives of the momentum tendency terms (Fig. 5). During stage 2, the
208 presence of friction (DIFF) produced shear that was positive across the front and against the
209 geostrophic shear, while the inertial response (CORI + PRES) had a tendency to decrease the
210 down-gradient shear and reinforce the along-front shear. During stage 3, winds rotated to the
211 upfront position and input shear against the geostrophic flow.

212 The terms in (4) were explored further using 1D+. The contribution from initial shear vs. friction
213 were evaluated by solving 1D+ for a) all terms in (4) (Fig. 6 b, f), b) no turbulence (i.e. no DIFF;
214 Fig. 6 c, g.) and c) no initial shear (Fig. 6 d, h). The vertical structure of shear from 2D (Fig. 6
215 a, e) and 1D+ (Fig. 6 b, f) highlight the important role of the inertial response and friction. An
216 oscillatory behavior existed deeper, indicative of waves (where only TEND and CORI dominate),
217 while contributions from the horizontal buoyancy gradient (PRES) and friction (DIFF) were seen
218 near the surface and throughout the ML. The case of no turbulence (Fig. 6 c, g.) was similar to in-
219 viscid adjustment (TG94), where the time dependent solution included inertial oscillations. Here,
220 the solution was modified by thermal wind imbalance set by the remnant shear from previous days
221 of wind forcing. This allowed for larger values and non-uniform shear within the ML compared to
222 the classic adjustment problem (which had a maximum shear of $2M^4f^{-2}$, TG94). The absence of
223 a damping term (by omitting friction, DIFF) implied the flow would continue as sheared inertial
224 oscillations. This was not the case when considering turbulence and unsteady forcing (Fig. 6 d, h).
225 Momentum input at the surface combined with the redistribution of momentum by DIFF simul-
226 taneously damped the inertial oscillation and introduced an external source of shear, also larger

227 than that of inviscid adjustment, particularly near the surface. The simplicity of (4) highlights the
228 importance of the transient frontal response to thermal wind imbalance resulting from the initial
229 shear and turbulence in the ML combined with unsteady wind forcing at the surface. These terms
230 worked in concert to evolve the shear.

231 The evolution of shear in 2D was matched by the 1D+ solution, and deviations point to the
232 importance of time varying viscosity and higher order terms in 2D (Wenegrat and McPhaden 2016;
233 Dauhajre and McWilliams 2018). Nonetheless, 1D+ captures the structure of shear predicted by
234 the more complex 2D during the time-span of the observations and suggests these are the dominant
235 terms modulating shear in the ML.

236 1D+ was also solved with initial conditions determined from OBS. Triaxus data at yd 216.3
237 provided an initial condition for Y and M^2 , while v was taken as the cross front averaged profile
238 from 2D. The agreement between the 1D+ solution and OBS is less obvious (Fig. 7). This may
239 be due to along front variability and curvature that influenced M^2 , as well as the semi Lagrangian
240 interpretation of the observations at depth (CCF1). Within the pycnocline (50 m), the solution and
241 observations exhibited similar oscillatory behavior, confirming that oscillations in the observations
242 (that also appear in 2D) were NIOs trapped below the ML. Yet near the surface, the agreement
243 between 1D+ and OBS is more complicated (Fig. 7 and Fig. 5). Agreement in cross-frontal shear
244 between OBS, 2D and 1D+ suggests the influence of friction (DIFF) during the restratification
245 phases stage 2 and 3. This was not the case in along front shear where OBS disagrees with 1D, 2D
246 and the friction term, but instead increases with the inertial terms (CORI + PRES). During stage
247 3, the model eroded the day-time near surface stratification while the OBS withstood erosion and
248 continued to stratify. This interaction between friction and stratification may explain part of the
249 discrepancy between the shear in 2D and OBS and is discussed in section 4b.

250 The 1D+ framework is a simple reduced set of coupled equations that explained the evolution of
 251 shear at this wind forced front similar to 2D. Specifically, 1D+, 2D and OBS all exhibited a positive
 252 cross front shear (Fig. 5). It will be shown that this cross front shear is able to differentially advect
 253 buoyancy across the front to enhance stratification comparable to the observations.

254 *b. Stratification*

255 The lack of an external strain field in 2D resulted in a weaker horizontal buoyancy gradient and
 256 therefore weaker vertical stratification than OBS. As such, the dominant source of stratification
 257 in 2D was from diurnal warming (compared to only $\sim 20\%$ of near surface stratification in OBS).
 258 To account for this discrepancy, the advective source of stratification in 1D+, 2D and OBS were
 259 isolated. In section 4a, the frontal response to turbulence and thermal wind imbalance induced a
 260 shear that differentially advected buoyancy across the front and modified vertical stratification. In
 261 CCF1, the amount of stratification from horizontal advection was estimated as

$$N_{ADV}^2 = \int_{t_o}^{t_i} -\frac{\partial b}{\partial x} \frac{\partial u}{\partial z} - \frac{\partial b}{\partial y} \frac{\partial v}{\partial z} dt. \quad (8)$$

262 Here, N_{ADV}^2 was solved for 1D+ with corresponding initial M^2 , and for 2D at each grid point.
 263 N_{ADV}^2 was also solved for the solution to TTW ($ifY = -M^2 + \partial^2(vY)/\partial z^2$; Gula et al. (2014))
 264 and for inviscid adjustment ADJ ($\partial Y/\partial t = -ifY - M^2$; TG94) at every grid point and averaged
 265 across the front. Results were non-dimensionalized in terms of balanced Richardson number $Ri_b =$
 266 $N^2 f^2 / M^4$, making comparison between the observations and 2D model simulations possible, since
 267 M^2 is almost an order of magnitude larger in OBS than in 2D. This also allows the results to be
 268 compared with the inviscid geostrophically adjusted state in TG94, where $N^2 = M^4 / f^2$, and $Ri_b = 1$
 269 (Fig. 8).

270 N_{ADV}^2 from 2D and the 1D+ solutions increased at rates similar to OBS, suggesting cross front
271 shear predicted by these idealized models were capable of reproducing the observed tilting of the
272 front. If the evolution was inviscid, as in TG94, shear would tilt isopycnals over and re-tilt them
273 back to vertical in an NIO. Conversely, if this was a case of TTW balance, the Ekman transport
274 and TTW circulation would stratify weakly at a rate unrelated to the tendency in the model and
275 observations.

276 The combination of terms encapsulated in (4; TEND, CORI, PRES and DIFF) suggest transient,
277 super inertial pressure gradient and frictional effects were responsible for advecting horizontal
278 stratification across the front. Without an external source of friction at the boundary, the ML shear
279 due to ADJ would damp out as momentum is distributed evenly throughout the water column
280 by friction. The surface boundary condition modified this further by providing an external input
281 of shear. The instantaneous magnitude and direction of friction at the surface was rotated as it
282 was distributed throughout the turbulent boundary layer by the DIFF term via unsteady Ekman
283 dynamics. This highlights the importance of friction and transience, both of which were needed
284 to produce a persistent flattening of isopycnals. This differentiates this simple 1D+ model and the
285 observations from traditional ADJ, slab ML NIOs, or balanced TTW.

286 This section brought together a simple reduced model of turbulent adjustment with an idealized
287 2D numerical simulation to highlight the role of unsteady wind forcing on the evolution of a
288 shallow ML front. Yet difference in the strength of ∇b between the OBS and 2D suggests the
289 importance of external circulation and along-front variability, which are excluded in the idealized
290 representations of the front and play an important role on the frontal structure.

291 c. Potential Vorticity

292 The role of different processes in setting the stratification can be seen through Ertel's form of
293 potential vorticity (PV)

$$q = (f\hat{\mathbf{z}} + \nabla \times \mathbf{u}) \cdot \nabla b. \quad (9)$$

294 Neglecting the contribution from vertical velocity, this can be written as a sum of the vertical and
295 horizontal components

$$q_v = (f + \zeta)N^2 \quad (10)$$

296

$$q_h = \frac{\partial u}{\partial z} \frac{\partial b}{\partial y} - \frac{\partial v}{\partial z} \frac{\partial b}{\partial x}. \quad (11)$$

297 CCF1 evaluated q_v and q_h in OBS and found that changes in these terms balanced each other in
298 the middle of the ML (16 m), illustrating PV conservation. This was not the case near the surface
299 (8 m) where q followed q_v as the near surface stratified, while the contribution from q_h remained
300 near zero. This increase of PV near the surface indicated the influence of PV injection on near
301 surface stratification.

302 Comparing PV in 2D vs OBS is obscured by underestimation of $|\nabla_h b|$ in 2D which resulted in
303 stratification dominated by heatflux rather than frontal tilting (Fig. 4). To account for this, PV
304 was calculated from 2D at 8 m (as in CCF1) using N_{ADV}^2 to isolate the contribution of friction
305 from that due to diabatic heating (Fig. 9). Downfront winds prior to the survey drove down PV
306 in the ML (Thomas 2005), resulting in negative PV at 8 m before the survey and during stage

307 1. As wind forcing subsided, shear developed as a result of adjustment as well as momentum
308 input at the surface that was redistributed in depth by friction (DIFF). The resulting cross frontal
309 shear advected buoyancy to increase N^2 and therefore PV through q_v . Note that cross front shear
310 did not impact q_h as the along front buoyancy gradient, by definition of the 2D model, was zero.

311 Therefore along front shear was the only term that influenced PV through q_h . In 2D, q_h increased

312 during stage 3, which was opposite of the observations (see CCF1, Fig. 14) where observed q_h
313 remains negative throughout the survey. This disagreement may be traced to the difference in along
314 front shear between OBS and 2D exhibited by the momentum budget terms (Fig. 5). This presents
315 a discrepancy between the along front shear in 2D and OBS. Nonetheless, the role of DIFF in the
316 redistribution of shear, and therefore in modulating q_h and q_v , confirms the importance of friction
317 on near surface PV.

318 5. Along Front Variability

319 Horizontal gradients observed in CCF1 increased in magnitude as smaller scales were resolved.
320 For example, an external strain field induced by the mesoscale circulation was documented by
321 an accompanying mesoscale survey Pallàs-Sanz et al. (2010b) and AVSIO (Archiving, Validation
322 and Interpretation of Satellite Oceanographic Data, <http://www.marine.copernicus.eu>). This
323 larger scale strain field was augmented by an internal strain field measured by OBS that modu-
324 lated with a meandering buoyancy field. This along front variability was apparent throughout the
325 observations and suggested by satellite SST (see CCF1, Fig. 1) that revealed wavelike structures
326 along the front. Wavelike patterns have been studied in many high resolution numerical simu-
327 lations as frontal instabilities (e.g., Capet et al. (2008)). Similar variability was captured by the
328 Triaxus survey in CCF1 and imprinted throughout fields of velocity, strain, vorticity and horizon-
329 tal buoyancy gradient. Strong horizontal gradients, meanders, and vertical velocity are all features
330 suggestive of growing baroclinic waves. In the ML, fronts exist in an environment of low stratifi-
331 cation and high Rossby number. This makes them susceptible to a type of ageostrophic baroclinic
332 instability (BCI) (Stone 1966; Boccaletti et al. 2007). These instabilities grow into eddies, mixed
333 layer eddies (MLE), that reach finite amplitude and stratification ensues. The rate of stratification
334 from MLE has been parameterized as an overturning streamfunction for coarse resolution models

335 (Fox-Kemper and Ferrari 2008; Fox-Kemper et al. 2008, 2011).

$$\Psi_o = C_e \frac{\nabla_h b H^2 \times \hat{\mathbf{z}}}{|f|} \mu(z) \quad (12)$$

$$\mu(z) = \left[1 - \left(\frac{2z}{H} + 1 \right)^2 \right] \left[1 + \frac{5}{21} \left(\frac{2z}{H} + 1 \right)^2 \right] \quad (13)$$

$$\frac{dN^2}{dt} = -C_e \frac{\nabla_h b^2 H^2}{|f|} \frac{\partial^2 \mu(z)}{\partial z^2} \quad (14)$$

338 Where C_e is a constant set to 0.06. A compelling feature of this parameterization is the vertical
339 structure of the overturning streamfunction $\mu(z)$, (analogous to that predicted by Eady (1949)), that
340 captures near surface intensification of MLE induced stratification (Fig. 10). N^2 predicted by this
341 parameterization developed a strikingly similar vertical structure as the observations, questioning
342 the possible role of mixed layer eddies as the source of stratification. Yet the parameterization
343 is meant to represent the along front and across front averages within an idealized model, and
344 not any instantaneous profile along the front. The OBS captured 5 km by 5 km averages of a
345 ~ 1 km wide front (e.g. Fig. 4) and did not necessarily average over a domain of vigorous eddies.
346 Furthermore, the parameterization as represented here does not account for the external strain field
347 or surface forcing, both of which modify the instability and frontal structure. While SST and in
348 situ data suggest frontal instability at this upwelling front, the results from sections 4a and 4b
349 demonstrate that adjustment modified by boundary layer turbulence was the mechanism driving
350 the superinertial slumping of the front.

351 A major discrepancy between 2D and OBS was the lack of strain field in 2D that resulted in
352 a broadening of the front compared with observations. Frontogenesis from baroclinic instability
353 would influence the magnitude of the horizontal buoyancy gradient and therefore stratification
354 resulting from the dynamics captured in (4). Therefore, the 3-D circulation magnifies the 2-D
355 effects described here. This brings attention to the importance of the external circulation and along
356 front variability at enhancing stratification as observed. Additionally, the similarity in stratification

³⁵⁷ predicted by MLE, the 2D model results (which inherently excludes MLE) and the observations
³⁵⁸ confirm the difficulties in separating different processes at ML fronts and is discussed in section 7.

³⁵⁹ 6. Buoyancy Flux Scalings

³⁶⁰ Many of the individual processes discussed throughout this manuscript have been identified as
³⁶¹ leading order in modulating stratification at fronts including: the effect of wind driven transport
³⁶² across a front (Ekman Bouyancy Flux, EBF, Thomas and Lee (2005)), TTW (Wenegrat et al. 2018;
³⁶³ McWilliams 2016), the transport of near inertial oscillations across a front (NIO EBF, Savel'yev
³⁶⁴ et al. (2018)) and MLE (Fox-Kemper and Ferrari 2008). These have been represented in the re-
³⁶⁵ spective literature as an equivalent surface buoyancy flux, \mathcal{B}_{eq} , which can be directly linked to the
³⁶⁶ energetics of the system and the stratification. Scalings of \mathcal{B}_{eq} were derived from a combination
³⁶⁷ of theory and idealized modeling, and presented in observationally accessible state variables. This
³⁶⁸ allows the restratifying/destratifying effects of these processes to be compared with each other and
³⁶⁹ with surface heating/cooling. A brief description and associated \mathcal{B}_{eq} are included in Table 1. A
³⁷⁰ more in depth discussion can be found in (McWilliams 2016) and references in Table 1.

³⁷¹ These scalings were calculated at this front using $\nabla_h b$, τ , from the observations, U_{NIO} from
³⁷² (6) and (7), an $H = 30$ m and $\rho_o = 1024$ kg m⁻³ (Fig. 11). The value for mixed layer eddies
³⁷³ (MLE) reach 3×10^{-6} m s⁻³. TTW scaling derived in Wenegrat et al. (2018) follows the same
³⁷⁴ parameter dependence as MLE (not shown). NIO EBF and surface heat flux (Q_{NET}) are orders
³⁷⁵ of magnitude less at $\sim 0.1 \times 10^{-6}$ m s⁻³. EBF suggests the importance of downfront winds in
³⁷⁶ the beginning of the survey and upfront winds towards the end. Observed \mathcal{B}_{eq} from CCF1 lie in
³⁷⁷ between at 1×10^{-6} m s⁻³. Though these values can be compared with each other, they do not
³⁷⁸ provide information about the likeliness of these dynamics occurring at this front. For example,
³⁷⁹ these scalings are associated with processes that occur on different time and spatial scales that

380 may not be appropriate for the localized nature of the observations and the rapid, superinertial
381 evolution of stratification. For example, EBF and TTW assume sub inertial timescales. Near
382 inertial oscillations (NIOs) describes the transport of a slab mixed layer, but does not necessarily
383 capture the differential shear within the ML that may tilt a front over. MLE and TTW scalings
384 were derived from a domain average over many fronts. Nonetheless, the observations and models
385 reveal evidence of all of these processes (e.g. friction, inertial response, frontogenesis) occurring
386 simultaneously to stratify the upper ocean rapidly within one inertial period.

387 **7. Vertical Structure of Stratification**

388 The external strain field was essential for strengthening ∇b and therefore the amount of N^2
389 by differential advection. This was evident when comparing the evolution of N^2 during stage 3
390 between OBS and 2D. The day-time N^2 in 2D was an order of magnitude less than OBS, and thus
391 was not strong enough to resist erosion by night-time mixing and convection. This was precisely
392 when N^2 in OBS increased the most.

393 The absence of night-time mixing in OBS during stage 3 highlights the importance of horizontal
394 processes on the upper ocean buoyancy budget and reinforces the role of external and internal
395 strain at influencing the strength of the front and therefore the magnitude of N^2 . The relationship
396 between horizontal buoyancy gradient and night-time mixing was explored by solving 1D+ for a
397 range of $|\nabla_h b|$. The resulting shear magnitude, $|\partial U / \partial z|$, and N_{ADV}^2 were used to estimate shear
398 Richardson number, $Ri_s = N^2 / |\partial U / \partial z|^2$, during night-time mixing (Fig. 12). Ri_s in 2D was sub-
399 critical (i.e. $Ri_s < 0.25$), with $Ri_s = 0.05$, compared to OBS, where $Ri_s = 4$. Stronger horizontal
400 gradients increase N_{ADV}^2 quadratically (through $\nabla_h b$ and $|\partial U / \partial z|$ via (4) and (8)). According to
401 this metric, a buoyancy gradient of $\sim \nabla_h b = 2 \times 10^{-7} \text{ s}^{-2}$ (compared to $\nabla_h b = 1.5 \times 10^{-6} \text{ s}^{-2}$ in
402 OBS) would be strong enough to maintain $Ri_s > 0.25$ and keep the upper ocean stratified as in the

403 observations. Therefore, the external 3-D circulation is essential for amplifying the 2-D effects on
404 stratification.

405 The observed stratification had a unique vertical structure that was enhanced near the surface
406 (Fig. 13). This vertical structure was replicated by N_{ADV}^2 from 2D and 1D+, suggesting these ide-
407 alized models were capturing differential advection by boundary layer turbulence enhanced near
408 the surface. This structure of stratification was also inherent in the MLE parameterization (14),
409 which shared the same behavior near the surface. The near surface enhancement of stratification
410 in 2D and MLE is traced to the dependence of $\partial N^2 / \partial t$ on $\partial^2 \mu(z) / \partial z^2$ in (14) and $\partial^2 v / \partial z^2$ in (4).
411 These both have a P-like vertical structure defined by (13) for $\mu(z)$ and the shape function for v in
412 KPP (Large et al. 1994). The shared character of stratification between the observations, theories,
413 and models demonstrates the complicated nature of teasing apart lateral processes in shallow ML.
414 The agreement in the structure of stratification would be different in very deep ML, where MLE
415 stratification would penetrate deeper (Mahadevan et al. 2012), while frictional dynamics would
416 dominate near the boundary (Wenegrat et al. 2018).

417 8. Discussion

418 This analysis describes the restratification of a front in the California Current System as a re-
419 sponse to a sudden decrease in winds. Similarly, the work of Dale et al. (2008) detailed the rapid
420 stratification of a shallow upwelling front after winds stopped and reversed direction. In that study,
421 it was concluded that an imbalance in the cross-shelf pressure gradient resulted in a rapid on shore
422 movement that steepened and slumped isopycnals simultaneously, therefore stratifying the ML on
423 an inertial timescale. Dale et al. (2008) compared the rapid slumping of isopycnals to a gravity cur-
424 rent, a process shown to occur at shallow ML fronts (i.e. Pham and Sarkar (2018)). Furthermore,
425 Dale et al. (2008) described the flow in context of near inertial oscillations, NIO (TEND, CORI,

426 DIFF) and adjustment, ADJ (TEND, PRES, CORI), but the combination of terms in (4) were not
427 explored. In the set of observations described here, the flow resembled a near inertial oscillation
428 (i.e. section 4), yet it was the full solution to (4) that captured the shear within the ML needed
429 to tilt the isopycnals over, highlighting the importance of frontal adjustment in the presence of
430 turbulence. As such, the initial shear in the ML when wind forcing stops along with the presence
431 of BL turbulence created ML stratification exceeding that predicted by inviscid adjustment.

432 Dauhajre and McWilliams (2018) found two stages of frontogenesis in the T3W problem. The
433 first stage documented the development of TTW by night-time mixing due to winds and convec-
434 tion. The other stage documented was a convergence field that developed as the change in velocity
435 (TEND) responded to the strength of horizontal buoyancy gradient (PRES) that changed across
436 the front. The result was a pulse of convergence on an inertial timescale that occurred daily with
437 the diurnal cycle (Dauhajre et al. 2017). This was similar to the mechanism explored by Dale et al.
438 (2008) that suggested differential slumping of isopycnals resulted in a sharpening of the front as it
439 tilted over. Both of these proposed mechanisms are consistent with the strengthening of the front
440 seen in OBS as wind forcing stops, and is different than the frontolytic forcing implied by the de-
441 formation field in the generalized omega equation approach determined by a concurrent mesoscale
442 survey (Pallàs-Sanz et al. 2010a). This presents a discrepancy between the temporal and spatial
443 interpretation of this rapidly evolving front. The competing frontogenetic and frontolytic effects
444 of BL turbulence (Gula et al. 2014; Bodner et al. 2019), advection (Dale et al. 2008; Dauhajre and
445 McWilliams 2018), and external/internal strain (Hoskins and Bretherton 1972; Shakespeare and
446 Taylor 2013; Barkan et al. 2019) play a key role in stratification at this front.

447 Furthermore, the surface stratification by differential advection converts horizontal changes of
448 salinity and temperature into vertical ones on a timescale that competes with surface forcing. If the
449 slumped gradients are subject to repeated mixing, they undergo a process of nonlinear diffusion

450 (Young 1994) that leads to horizontal density compensation often observed in the ML (Rudnick
451 1999). This might provide a mechanism to homogenize the cold salty, recently upwelled waters
452 with the warmer, fresher surface waters offshore, and therefore an important part in the mixing of
453 tracers in the California Current System upwelling regime.

454 9. Conclusion

455 Detailed observations combined with idealized models show the importance of horizontal advec-
456 tion in stratifying the upper ocean. Specifically, an idealized 2-D model combined with a simple
457 reduced model, 1D+, were able to give insight into the role of turbulent adjustment that can rapidly
458 stratify the ML on superinertial timescales and compete with surface forcing. Additionally, im-
459 ages of SST and along front variability captured in the observations suggest possible mixed layer
460 instabilities, which grow on a relatively longer timescale, suggesting that this rapid stratification
461 was dominated by turbulent adjustment.

462 The vertical structure of stratification reveals the importance of boundary layer dynamics on
463 shallow ML fronts. Traditionally, attention has been given to the importance of fronts in deep
464 MLs, as they have stored potential energy available to grow instabilities. Here demonstrates a
465 mechanism of rapid restratification that can be dominant in shallow MLs and act to decrease
466 the available potential energy faster than predicted from mixed layer baroclinic instability. This
467 suggests the potential importance of shallow MLs on the upper ocean buoyancy budget (Johnson
468 et al. 2016), where sharp fronts exist and therefore compensate for shallow ML depths.

469 None of the current scalings or parameterizations capture this rapid stratification (e.g. Table 1).
470 NIO (Savelyev et al. 2018) has been used to explain the integrated Ekman transport of NIO over the
471 deeper Gulf Stream, but does not provide information on shear within the boundary layer, which
472 in this study is responsible for the stratification in OBS and 2D. EBF (Thomas and Lee 2005) and

473 TTW (McWilliams et al. 2015; Wenegrat et al. 2018) demonstrate the importance of friction and
474 viscosity on thermal wind balance, but assume subinertial timescales. In other words, the time
475 dependent adjustment is missing friction, and the friction scalings are not capturing transient shear
476 due to unsteady winds. The observations combined with the model simulation presented here
477 show that both are important for predicting the restratification at this shallow surface intensified
478 front. The abundance of fronts in the upper ocean and the transience of surface forcing on the ML
479 implies the dynamics explored here have implications for better representing fluxes of momentum,
480 heat and gas exchange between the ocean and atmosphere.

481 *Acknowledgments.* This work was supported by Office of Naval Research Grants N00014-05-1-
482 0329 and N00014-09-1-0266. We thank Daniel Dauhajre for constructive discussions regarding
483 transient turbulent thermal wind. Insightful comments by Eric Kunze and two anonymous review-
484 ers greatly improved the manuscript.

485 APPENDIX

486 **Configuration of the MITgcm**

487 The MITgcm (Marshall et al. 1997) was run in hydrostatic mode with a horizontally periodic
488 domain extending 600 m in the along front direction and 191700 m across the front. The hori-
489 zontal resolution was 300 m, allowing 2 grid points along the front and 639 grid points across the
490 front. The vertical resolution was a uniform 3 m extending to 150 m depth. Horizontal mixing of
491 momentum was parameterized using a bi-harmonic operator, with a Smagorinsky coefficient of 3,
492 and Leith and modified Leith coefficients of 1. KPP was chosen for the vertical mixing scheme.

493 The model was initialized in the periodic domain using a geostrophically balanced double-front
 494 configuration, with a horizontal structure given by:

$$Y(y) = \begin{cases} 0.5 \left[1 - \tanh\left(\frac{y}{L_f}\right) + \tanh\left(\frac{y-L_y/2}{L_f}\right) \right] \left(\tanh\left(\frac{z+2H}{H}\right) + 1 \right), & 0 \leq y \leq L_y/2, \\ 0.5 \left[\tanh\left(\frac{y-L_y/2}{L_f}\right) - \tanh\left(\frac{y-L_y}{L_f}\right) - 1 \right] \left(\tanh\left(\frac{z+2H}{H}\right) + 1 \right), & L_y/2 \leq y \leq L_y, \end{cases}$$

495 This horizontal structure was then fit to the observed data to obtain a vertical structure using:

$$T = \Delta T_o Y(y) + \Gamma_T(z)$$

$$S = -\Delta S_o Y(y) + \Gamma_S(z)$$

496 where $\Delta T_o = 1.6 \text{ } ^\circ\text{C}$, $\Delta S_o = 0.5 \text{ g kg}^{-1}$ and $\Gamma_T(z)$ and $\Gamma_S(z)$ were:

$$\Gamma_T(z) = 0.4932e^{\left(-8.46667 \times 10^{-6} \frac{z}{L_z}\right)} + 0.5993e^{\left(-1.7820 \times 10^{-4} \frac{z}{L_z}\right)}$$

$$\Gamma_S(z) = 0.0710e^{\left(-5.5373 \times 10^{-5} \frac{z}{L_z}\right)} + 1.0980e^{\left(-3.1193 \times 10^{-7} \frac{z}{L_z}\right)}$$

497 Density was calculated assuming a linear equation of state $\rho = \rho_o + \rho_o(-\alpha_T(T - T_o) + \beta(S -$
 498 $S_o))$, with $\alpha = 2.1766 \times 10^{-4} \text{ K}^{-1}$ and $\beta = 7.4137 \times 10^{-4} \text{ kg g}^{-1}$, $T_o = 15.8 \text{ } ^\circ\text{C}$ and $S_o = 33.1$
 499 g kg^{-1} . The initial model domain can be seen in Fig. A1. Although the MITgcm configuration
 500 contained three dimensions, the use of only two grid point in the along front direction prevents
 501 along front variability while allowing cross frontal variability. It was therefore interpreted as a
 502 2-D configuration.

503 References

504 Barkan, R., M. J. Molemaker, K. Srinivasan, J. C. McWilliams, and E. A. D'Asaro, 2019:
 505 The Role of Horizontal Divergence in Submesoscale Frontogenesis. *Journal of Physical*
 506 *Oceanography*, **49** (6), 1593–1618, doi:10.1175/JPO-D-18-0162.1, URL <https://doi.org/10.1175/JPO-D-18-0162.1>.

- 508 Boccaletti, G., R. Ferrari, and B. Fox-Kemper, 2007: Mixed Layer Instabilities and Restrati-
509 cation. *Journal of Physical Oceanography*, **37** (9), 2228–2250, doi:10.1175/JPO3101.1, URL
510 <https://doi.org/10.1175/JPO3101.1><http://journals.ametsoc.org/doi/abs/10.1175/JPO3101.1>.
- 511 Bodner, A. S., B. Fox-Kemper, L. P. Van Roekel, J. C. McWilliams, and P. P. Sullivan, 2019: A per-
512 turbation approach to understanding the effects of turbulence on frontogenesis. *Journal of Fluid
513 Mechanics*, **883**, A25, doi:DOI:10.1017/jfm.2019.804, URL <https://www.cambridge.org/core/article/perturbation-approach-to-understanding-the-effects-of-turbulence-on-frontogenesis/02E4D757B3B0E97EEBBD11B7CB174A5B>.
- 515 Capet, X., J. C. McWilliams, M. J. Molemaker, and A. F. Shchepetkin, 2008: Mesoscale to Sub-
516 mesoscale Transition in the California Current System. Part I: Flow Structure, Eddy Flux,
517 and Observational Tests. *Journal of Physical Oceanography*, **38** (1), 29–43, doi:10.1175/
518 2007JPO3671.1, URL <https://doi.org/10.1175/2007JPO3671.1><http://journals.ametsoc.org/doi/abs/10.1175/2007JPO3671.1>.
- 520 Cronin, M. F., and W. S. Kessler, 2009: Near-Surface Shear Flow in the Tropical Pacific
521 Cold Tongue Front*. *Journal of Physical Oceanography*, **39** (5), 1200–1215, doi:10.1175/
522 2008JPO4064.1, URL <https://doi.org/10.1175/2008JPO4064.1><http://journals.ametsoc.org/doi/abs/10.1175/2008JPO4064.1>.
- 524 Dale, A. C., J. A. Barth, M. D. Levine, and J. A. Austin, 2008: Observations of mixed layer
525 restratification by onshore surface transport following wind reversal in a coastal upwelling re-
526 gion. *Journal of Geophysical Research*, **113** (C1), C01 010, doi:10.1029/2007JC004128, URL
527 <https://doi.org/10.1029/2007JC004128><http://doi.wiley.com/10.1029/2007JC004128>.
- 528 Dauhajre, D. P., and J. C. McWilliams, 2018: Diurnal Evolution of Submesoscale Front and
529 Filament Circulations. *Journal of Physical Oceanography*, **48** (10), 2343–2361, doi:10.1175/
530

- 531 JPO-D-18-0143.1, URL <https://doi.org/10.1175/JPO-D-18-0143.1>
532 http://journals.ametsoc.org/doi/10.1175/JPO-D-18-0143.1.
- 533 Dauhajre, D. P., J. C. McWilliams, and Y. Uchiyama, 2017: Submesoscale Coherent Structures
534 on the Continental Shelf. *Journal of Physical Oceanography*, **47** (12), 2949–2976, doi:10.1175/
535 JPO-D-16-0270.1, URL <https://doi.org/10.1175/JPO-D-16-0270.1>
536 http://journals.ametsoc.org/doi/10.1175/JPO-D-16-0270.1.
- 537 Eady, E. T., 1949: Long Waves and Cyclone Waves. *Tellus*, **1** (3), 33–52, doi:10.3402/tellusa.v1i3.
538 8507, URL <https://doi.org/10.3402/tellusa.v1i3.8507>https://www.tandfonline.com/doi/full/10.
539 3402/tellusa.v1i3.8507.
- 540 Farrar, J. T., C. J. Zappa, R. A. Weller, and A. T. Jessup, 2007: Sea surface temperature signatures
541 of oceanic internal waves in low winds. *Journal of Geophysical Research*, **112** (C6), C06014,
542 doi:10.1029/2006JC003947, URL <http://doi.wiley.com/10.1029/2006JC003947>.
- 543 Fox-Kemper, B., and R. Ferrari, 2008: Parameterization of Mixed Layer Eddies. Part II:
544 Prognosis and Impact. *Journal of Physical Oceanography*, **38** (6), 1166–1179, doi:10.1175/
545 2007JPO3788.1, URL <https://doi.org/10.1175/2007JPO3788.1>http://journals.ametsoc.org/doi/
546 abs/10.1175/2007JPO3788.1.
- 547 Fox-Kemper, B., R. Ferrari, and R. Hallberg, 2008: Parameterization of Mixed Layer Eddies.
548 Part I: Theory and Diagnosis. *Journal of Physical Oceanography*, **38** (6), 1145–1165, doi:
549 10.1175/2007JPO3792.1, URL <https://doi.org/10.1175/2007JPO3792.1>http://journals.ametsoc.
550 org/doi/abs/10.1175/2007JPO3792.1.
- 551 Fox-Kemper, B., and Coauthors, 2011: Parameterization of mixed layer eddies. III: Imple-
552 mentation and impact in global ocean climate simulations. *Ocean Modelling*, **39** (1-2),

- 553 61–78, doi:10.1016/j.ocemod.2010.09.002, URL <https://linkinghub.elsevier.com/retrieve/pii/S1463500310001290>.
- 554
- 555 Gula, J., M. J. Molemaker, and J. C. McWilliams, 2014: Submesoscale Cold Filaments in the Gulf
556 Stream. *Journal of Physical Oceanography*, **44** (10), 2617–2643, doi:10.1175/JPO-D-14-0029.
- 557 1, URL <http://journals.ametsoc.org/doi/abs/10.1175/JPO-D-14-0029.1>.
- 558 Hosegood, P., M. C. Gregg, and M. H. Alford, 2006: Sub-mesoscale lateral density structure
559 in the oceanic surface mixed layer. *Geophysical Research Letters*, **33** (22), L22 604, doi:
560 10.1029/2006GL026797, URL <https://doi.org/10.1029/2006GL026797><http://doi.wiley.com/10.1029/2006GL026797>.
- 561
- 562 Hoskins, B. J., and F. P. Bretherton, 1972: Atmospheric frontogenesis models: Mathematical
563 formulation and solution. *Journal of the Atmospheric Sciences*, **29** (1),
564 11–37, doi:10.1175/1520-0469(1972)029<0011:AFMMFA>2.0.CO;2, URL [https://doi.org/10.1175//doi.org/10.1175/1520-0469\(1972\)029<0011:AFMMFA>2.0.CO;2](https://doi.org/10.1175//doi.org/10.1175/1520-0469(1972)029<0011:AFMMFA>2.0.CO;2),
565 [https://doi.org/10.1175/1520-0469\(1972\)029<0011:AFMMFA>2.0.CO;2](https://doi.org/10.1175/1520-0469(1972)029<0011:AFMMFA>2.0.CO;2), [https://doi.org/10.1175/1520-0469\(1972\)029<0011:AFMMFA>2.0.CO;2](https://doi.org/10.1175/1520-0469(1972)029<0011:AFMMFA>2.0.CO;2).
- 566
- 567 Johnson, L., C. M. Lee, and E. A. D’Asaro, 2016: Global Estimates of Lateral Spring-
568 time Restratification. *Journal of Physical Oceanography*, **46** (5), 1555–1573, doi:10.1175/
569 JPO-D-15-0163.1, URL <https://doi.org/10.1175/JPO-D-15-0163.1><http://journals.ametsoc.org/doi/10.1175/JPO-D-15-0163.1>.
- 570
- 571 Large, W. G., J. C. McWilliams, and S. C. Doney, 1994: Oceanic vertical mixing: A review
572 and a model with a nonlocal boundary layer parameterization. *Reviews of Geophysics*, **32** (4),
573 363, doi:10.1029/94RG01872, URL <https://doi.org/10.1029/94RG01872><http://doi.wiley.com/10.1029/94RG01872>.
- 574

- 575 LeVeque, R. J., 2007: *Finite Difference Methods for Ordinary and Partial Differential Equations,*
576 *Steady State and Time Dependent Problems.* SIAM, Philadelphia.
- 577 Lévy, M., P. Klein, A.-M. Tréguier, D. Iovino, G. Madec, S. Masson, and K. Takahashi, 2010:
578 Modifications of gyre circulation by sub-mesoscale physics. *Ocean Modelling*, **34** (1-2), 1–
579 15, doi:10.1016/j.ocemod.2010.04.001, URL <http://www.sciencedirect.com/science/article/pii/S1463500310000582>.
580
- 581 Mahadevan, A., E. D'Asaro, C. Lee, and M. J. Perry, 2012: Eddy-Driven Stratification Initiates
582 North Atlantic Spring Phytoplankton Blooms. *Science*, **337** (6090), 54–58, doi:10.1126/science.
583 1218740, URL <http://science.sciencemag.org/content/337/6090/54> http://www.sciencemag.org/
584 lookup/doi/10.1126/science.1218740.
- 585 Marshall, J., A. Adcroft, C. Hill, L. Perelman, and C. Heisey, 1997: A finite-volume, incom-
586 pressible Navier Stokes model for studies of the ocean on parallel computers. *Journal of
587 Geophysical Research: Oceans*, **102** (C3), 5753–5766, doi:10.1029/96JC02775, URL <https://doi.org/10.1029/96JC02775> http://doi.wiley.com/10.1029/96JC02775.
- 588
- 589 McWilliams, J. C., 2016: Submesoscale currents in the ocean. *Proceedings of the Royal Soci-
590 ety A: Mathematical, Physical and Engineering Sciences*, **472** (2189), 20160117, doi:10.1098/
591 rspa.2016.0117, URL <https://royalsocietypublishing.org/doi/abs/10.1098/rspa.2016.0117> https://
592 royalsocietypublishing.org/doi/10.1098/rspa.2016.0117.
- 593
- 594 McWilliams, J. C., J. Gula, M. J. Molemaker, L. Renault, and A. F. Shchepetkin, 2015:
595 Filament Frontogenesis by Boundary Layer Turbulence. *Journal of Physical Oceanog-
596 raphy*, **45** (8), 1988–2005, doi:10.1175/JPO-D-14-0211.1, URL <https://doi.org/10.1175/JPO-D-14-0211.1> http://journals.ametsoc.org/doi/10.1175/JPO-D-14-0211.1.

- 597 McWilliams, J. C., and E. Huckle, 2006: Ekman Layer Rectification. *Journal of Physical*
598 *Oceanography*, **36** (8), 1646–1659, doi:10.1175/JPO2912.1, URL <http://journals.ametsoc.org/doi/abs/10.1175/JPO2912.1>.
- 600 Pallàs-Sanz, E., T. M. S. Johnston, and D. L. Rudnick, 2010a: Frontal dynamics in a California
601 Current System shallow front: 1. Frontal processes and tracer structure. *Journal of Geophysical Research*, **115** (C12), C12 067, doi:10.1029/2009JC006032, URL <https://doi.org/10.1029/2009JC006032> <http://doi.wiley.com/10.1029/2009JC006032>.
- 604 Pallàs-Sanz, E., T. M. S. Johnston, and D. L. Rudnick, 2010b: Frontal dynamics in a California
605 Current System shallow front: 2. Mesoscale vertical velocity. *Journal of Geophysical Research*, **115** (C12), C12 068, doi:10.1029/2010JC006474, URL <https://doi.org/10.1029/2010JC006474> <http://doi.wiley.com/10.1029/2010JC006474>.
- 608 Pham, H. T., and S. Sarkar, 2018: Ageostrophic Secondary Circulation at a Submesoscale Front
609 and the Formation of Gravity Currents. *Journal of Physical Oceanography*, **48** (10), 2507–2529,
610 doi:10.1175/JPO-D-17-0271.1, URL <https://doi.org/10.1175/JPO-D-17-0271.1>.
- 614 Pollard, R., and R. Millard, 1970: Comparison between observed and simulated wind-
615 generated inertial oscillations. *Deep Sea Research and Oceanographic Abstracts*, **17** (4), 813–
616 821, doi:10.1016/0011-7471(70)90043-4, URL <http://www.sciencedirect.com/science/article/pii/0011747170900434> <https://linkinghub.elsevier.com/retrieve/pii/0011747170900434>.
- 618 Price, J. F., R. A. Weller, and R. Pinkel, 1986: Diurnal cycling: Observations and models of
619 the upper ocean response to diurnal heating, cooling, and wind mixing. *Journal of Geophysical Research*, **91** (C7), 8411, doi:10.1029/JC091iC07p08411, URL <https://doi.org/10.1029/JC091iC07p08411> <http://doi.wiley.com/10.1029/JC091iC07p08411>.

- 619 Rudnick, D. L., 1999: Compensation of Horizontal Temperature and Salinity Gradients
620 in the Ocean Mixed Layer. *Science*, **283** (5401), 526–529, doi:10.1126/science.283.5401.526.
621 URL <http://science.sciencemag.org/content/283/5401/526>
622 URL <http://www.sciencemag.org/cgi/doi/10.1126/science.283.5401.526>.
- 623 Saveliyev, I., and Coauthors, 2018: Aerial Observations of Symmetric Instability at the
624 North Wall of the Gulf Stream. *Geophysical Research Letters*, **45** (1), 236–244, doi:
625 10.1002/2017GL075735, URL <https://doi.org/10.1002/2017GL075735>
626 URL <http://doi.wiley.com/10.1002/2017GL075735>.
- 627 Shakespeare, C. J., and J. R. Taylor, 2013: A generalized mathematical model of geostrophic
628 adjustment and frontogenesis: uniform potential vorticity. *Journal of Fluid Mechanics*,
629 **736**, 366–413, doi:DOI:10.1017/jfm.2013.526, URL <https://www.cambridge.org/core/article/generalized-mathematical-model-of-geostrophic-adjustment-and-frontogenesis-uniform-potential-vortic/809C48C22ED63CE88E1CCAF715D22343>.
- 630
- 631 Stone, P. H., 1966: On Non-Geostrophic Baroclinic Stability. *Journal of the Atmospheric
632 Sciences*, **23** (4), 390–400, doi:10.1175/1520-0469(1966)023<0390:ONGBS>2.0.CO;2, URL
633 [https://doi.org/10.1175/1520-0469\(1966\)023%3C0390:ONGBS%3E2.0.CO2](https://doi.org/10.1175/1520-0469(1966)023%3C0390:ONGBS%3E2.0.CO2)
634 URL <http://journals.ametsoc.org/doi/abs/10.1175/1520-0469%281966%29023%3C0390%3AONGBS%3E2.0.CO%2B2>.
- 635
- 636
- 637 Su, Z., J. Wang, P. Klein, A. F. Thompson, and D. Menemenlis, 2018: Ocean submesoscales
638 as a key component of the global heat budget. *Nature Communications*, **9** (1), 775, doi:
639 10.1038/s41467-018-02983-w, URL <https://doi.org/10.1038/s41467-018-02983-w>
640 URL <http://www.nature.com/articles/s41467-018-02983-w>.

- 641 Tandon, A., and C. Garrett, 1994: Mixed Layer Restratification Due to a Horizontal
642 Density Gradient. *Journal of Physical Oceanography*, **24** (6), 1419–1424, doi:
643 10.1175/1520-0485(1994)024<1419:MLRDTA>2.0.CO;2, URL [https://doi.org/10.1175/1520-0485\(1994\)024{\%}3C1419:MLRDTA{\%}3E2.0.CO2](https://doi.org/10.1175/1520-0485(1994)024{\%}3C1419:MLRDTA{\%}3E2.0.CO2)
644 <http://journals.ametsoc.org/doi/abs/10.1175/1520-0485{\%}281994{\%}29024{\%}3C1419{\%}3AMLRDTA{\%}3E2.0.>
645 CO{\%}3B2.
646
- 647 Thomas, L. N., 2005: Destruction of Potential Vorticity by Winds. *Journal of Physical Oceanogra-*
648 *phy*, **35** (12), 2457–2466, doi:10.1175/JPO2830.1, URL <https://doi.org/10.1175/JPO2830.1>
649 <http://journals.ametsoc.org/doi/abs/10.1175/JPO2830.1>.
- 650 Thomas, L. N., and C. M. Lee, 2005: Intensification of Ocean Fronts by Down-Front Winds.
651 *Journal of Physical Oceanography*, **35** (6), 1086–1102, doi:10.1175/JPO2737.1, URL <https://doi.org/10.1175/JPO2737.1>
652 <http://journals.ametsoc.org/doi/abs/10.1175/JPO2737.1>.
- 653 Thompson, A. F., A. Lazar, C. Buckingham, A. C. Naveira Garabato, G. M. Damerell, and K. J.
654 Heywood, 2016: Open-Ocean Submesoscale Motions: A Full Seasonal Cycle of Mixed Layer
655 Instabilities from Gliders. *Journal of Physical Oceanography*, **46** (4), 1285–1307, doi:10.1175/
656 JPO-D-15-0170.1, URL <https://doi.org/10.1175/JPO-D-15-0170.1>
657 <http://journals.ametsoc.org/doi/10.1175/JPO-D-15-0170.1>.
- 658 Timmermans, M.-L., and P. Winsor, 2013: Scales of horizontal density structure in the Chukchi
659 Sea surface layer. *Continental Shelf Research*, **52**, 39–45, doi:10.1016/j.csr.2012.10.015,
660 URL <http://www.sciencedirect.com/science/article/pii/S0278434312002919>
661 <https://linkinghub.elsevier.com/retrieve/pii/S0278434312002919>.
- 662 Van de Wiel, B. J. H., A. F. Moene, G. J. Steeneveld, P. Baas, F. C. Bosveld, and A. A. M. Holtslag,
663 2010: A Conceptual View on Inertial Oscillations and Nocturnal Low-Level Jets. *Journal of the*

- 664 *Atmospheric Sciences*, **67** (8), 2679–2689, doi:10.1175/2010JAS3289.1, URL <https://doi.org/10.1175/2010JAS3289.1>
665 <http://journals.ametsoc.org/doi/abs/10.1175/2010JAS3289.1>.
- 666 Wenegrat, J. O., and M. J. McPhaden, 2016: Wind, Waves, and Fronts: Frictional Effects in a
667 Generalized Ekman Model*. *Journal of Physical Oceanography*, **46** (2), 371–394, doi:10.1175/
668 [JPO-D-15-0162.1](http://journals.ametsoc.org/doi/10.1175/JPO-D-15-0162.1), URL <http://journals.ametsoc.org/doi/10.1175/JPO-D-15-0162.1>.
- 669 Wenegrat, J. O., L. N. Thomas, J. Gula, and J. C. McWilliams, 2018: Effects of the Sub-
670 mesoscale on the Potential Vorticity Budget of Ocean Mode Waters. *Journal of Physical
671 Oceanography*, **48** (9), 2141–2165, doi:10.1175/JPO-D-17-0219.1, URL <https://doi.org/10.1175/JPO-D-17-0219.1>
672 <http://journals.ametsoc.org/doi/10.1175/JPO-D-17-0219.1>.
- 673 Young, W. R., 1994: The Subinertial Mixed Layer Approximation. *Journal of Physical Oceanog-
674 raphy*, **24** (8), 1812–1826, doi:10.1175/1520-0485(1994)024<1812:TSMLA>2.0.CO;2, URL
675 [https://doi.org/10.1175/1520-0485\(1994\)024{\%}3C1812:TSMLA{\%}3E2.0.CO2](https://doi.org/10.1175/1520-0485(1994)024{\%}3C1812:TSMLA{\%}3E2.0.CO2)
676 <http://journals.ametsoc.org/doi/abs/10.1175/1520-0485{\%}281994{\%}29024{\%}3C1812{\%}3A>
677 <http://journals.ametsoc.org/doi/abs/10.1175/1520-0485{\%}3E2.0.CO{\%}3B2>.

678 LIST OF TABLES

679	Table 1. Scalings of $w'b'$ for relevant processes shown to influence stratification at upper	
680	ocean fronts.	33

TABLE 1. Scalings of $w'b'$ for relevant processes shown to influence stratification at upper ocean fronts.

	$w'b'$	Description	Reference
Mixed Layer Eddies	$0.06 \frac{\nabla_h b^2 H^2}{f}$	Baroclinic instability of a mixed layer front	Fox-Kemper et. al. 2008
Ekman Buoyancy Flux	$\frac{\tau \times \nabla_h b^2}{\rho f}$	Ekman transport across the front	Thomas and Lee 2005
Near Inertial Oscillation	$U_{NIO} \cdot \nabla_h b$	Near-inertial transport across the front	Savelyev et al. 2017
Heat Flux	$Q \frac{\alpha g}{\rho c_p}$	Vertical flux of buoyancy from heat at surface	—

681 LIST OF FIGURES

- Fig. 1.** The vertical structure of the ML for 1D (1st column), 2D (2nd column) and OBS. Rows are stratification, cross front velocity and cross front shear, respectively. The last row contains surface forcing used in 1D and 2D. Dashed lines separate the different stages 1–3 outlined in section 1. Specifically: a) 1D N^2 with PWP ML (grey dots), b) 2D N^2 with KPP boundary layer depth (grey dots), c) OBS N^2 with float depth (grey dots), d) 1D u^{xf} , e) 2D u^{xf} , f) OBS u , g) 1D u_z^{xf} , h) 2D u_z^{xf} , i) OBS u_z , j) QNET, k) τ^{af} (grey) and τ^{xf} (black), l) ML average viscosity ν

Fig. 2. Vertical gradients predicted by 1D (purple) compared with those observed by the float (blue), Triaxus at 4 m (orange) and Triaxus at 12 m. Variables include (a) b , (b) T , and (c) S . Dashed lines separate the different stages 1–3 outlined in section 1. 36

Fig. 3. NIO at the front as a response to a sudden decrease in winds. a) Wind stress starting 3 days after the start of 2D and 2 days before the survey began, τ^{af} is blue and τ^{xf} is purple. b) Plan view of surface ρ in 2D as a function of cross front distance and time. Grey lines are isopycnals, and black dots are the cross front distance of the float trajectory overlaid for reference. Surface velocity from 2D (purple), the solution to (6) and (7) (grey), and OBS (orange) for c) u^{xf} in models and u in OBS, d) u^{af} and - v in OBS and e) $|U|$ for model and OBS. 38

Fig. 4. Cross front density structure from OBS compared with 2D. The initial Triaxus transect (obs T₁, dark green) crossed the entire front. Triaxus while following the float (obs >T₂, light green) surveyed the sharpest part of the front. 2D after one time step, 6 days before OBS (model T₀, dark purple). Cross frontal structure in 2D at the start of the Lagrangian survey (model T₁, light purple) after 6 days of wind forcing. 39

Fig. 5. (a) Cross front shear u_z^{xf} and (b) along front shear u_z^{af} . In 2D (grey), 1D+ (purple), and OBS (orange). The contribution of the inertial terms, CORI + PRES (red) and friction, DIFF (teal) to the shear budget in 2D are also included. 40

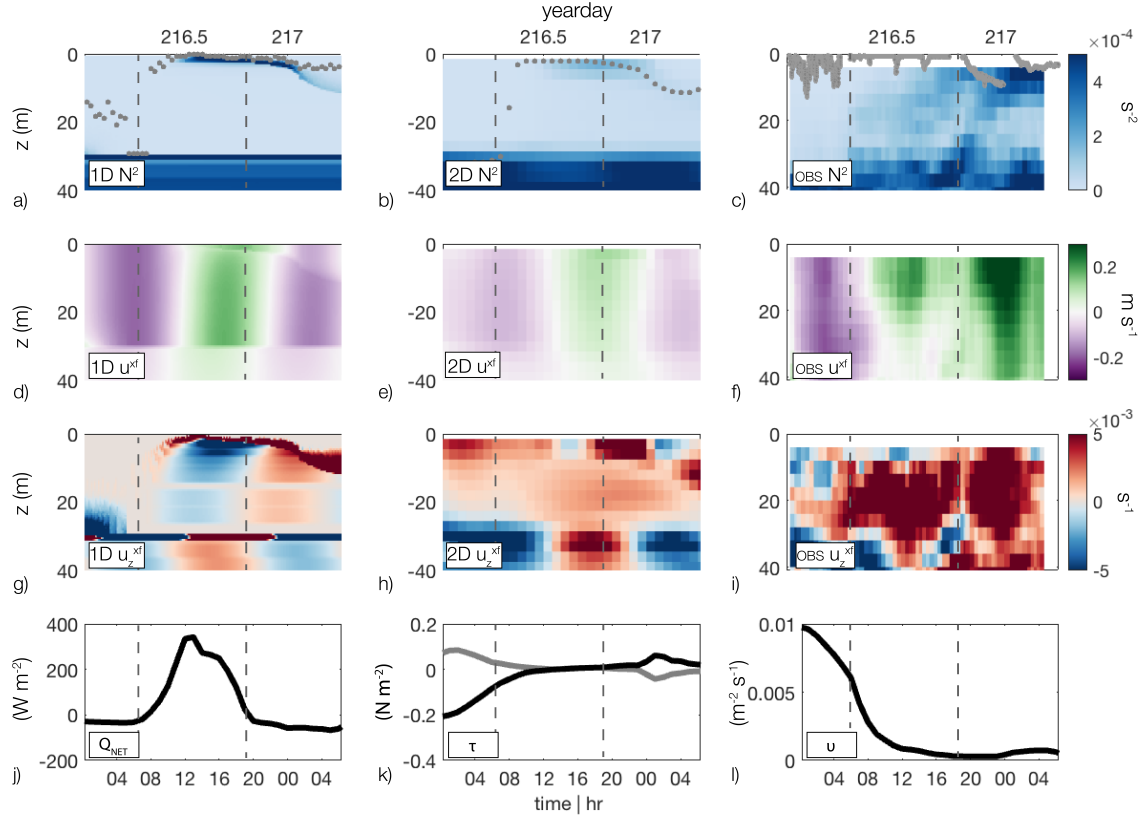
Fig. 6. Along front shear (AF - left panels) and cross front shear (CF - right panels) predicted by 2D (a, c), 1D+ (b, d), 1D+ without friction (e, g) and 1D+ without initial shear (f, h). Specifically: a) AF - 2D, b) AF - 1D+, c) XF - 2D, d) XF - 1D+, e) AF - 1D+ no DIFF, f) AF - 1D+ no Y_o , g) XF - 1D+ no DIFF, h) XF - 1D+ no Y_o . Float depth from OBS (grey dots) are included for reference. 41

Fig. 7. Vertical shear predicted by 1D+ (initialized with OBS at the beginning of stage 2) compared with OBS. Only stage 2 and 3 are shown. a) 1D+ zonal shear, b) 1D+ meridional shear c) OBS zonal shear, d) OBS meridional shear. 42

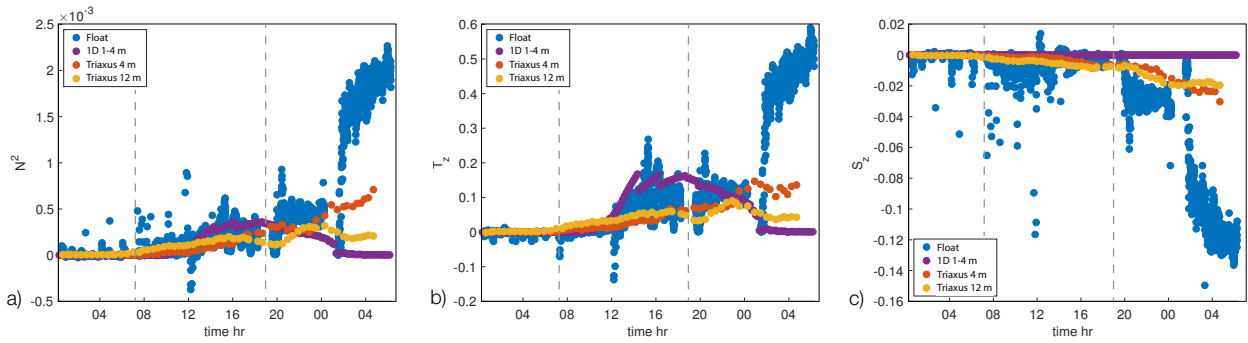
Fig. 8. N^2 (normalized to Ri_B) predicted by different models compared to the observations. N^2 from OBS and N_{ADV}^2 for the 1D+ solution to OBS are in dark green and light green, respectively. N_{ADV}^2 in 2D and the 1D+ solution to 2D are in dark purple and light purple, respectively. Also included are N_{ADV}^2 from 1D+ solutions to ADJ (TEND, ADV, PRES - orange) and TTW (ADV, PRES, DIFF - yellow). 43

Fig. 9. PV at 8 m from 2D using N_{ADV}^2 to isolate changes resulting from vertical shear. Total q (black), horizontal q_h (green) and vertical q_v (blue). Grey dashed lines are the PV associated with thermal wind balance $q_{hg} = -b_{xf}^2/f$ (grey dashed lines). The observed float depth (scaled $\times 10^{-10}$) is included for reference. 44

724	Fig. 10. Observed N^2 compared with that predicted by the MLE parameterization. a) N^2 from OBS 725 in depth and time calculated from the Triaxus. Float position (grey dots) are included for 726 reference. b) N^2 estimated from (14). Grey dashed lines represent the division between 727 stages.	45
728	Fig. 11. Scalings of $w'b'$ (left axis) and effective Q_{NET} (right axis) for MLI (red), EBF (green), NIO 729 EBF (yellow) and observed Q_{NET} (purple). Values were calculated as in Table 1 using 730 observed ∇b_h , H , f , τ and solutions to (6) and (7). Average $w'b'$ derived from the observed 731 N^2 is included for reference (grey dashed line).	46
732	Fig. 12. Comparison between shear Richardson number, Ri_s , and horizontal buoyancy gradient 733 $ \nabla_h b $. Ri_s was calculated during stage 3 (night-time mixing) from OBS (green), from 2D 734 (dark purple) and from the solution to 1D+ for varying M^2 (light purple). The dashed grey 735 line corresponds to critical $Ri_s = 0.25$	47
736	Fig. 13. Vertical structure of N^2 in terms of Ri_b predicted by different models compared with obser- 737 vations (e.g. see Fig. 8 and Fig. 10). N^2 from OBS and N_{ADV}^2 from 1D+ initiated with OBS 738 are in dark green and light green, respectively. N_{ADV}^2 from 2D and 1D+ initiated with 2D are 739 in dark purple and light purple, respectively. N^2 predicted from MLI using (14) is in blue.	48
740	Fig. A1. Initial density structure in MITgcm. The along front distance is 600 m (2 grid points) with 741 a cross front direction of 191700 m (639 grid points) and a horizontal resolution of 300 m. 742 The vertical resolution was 3 m extending to 150 m depth. The cross frontal density (scaled) 743 is plotted above the front for visual reference. For an exact cross front density structure, see 744 Fig. 4	49



745 FIG. 1. The vertical structure of the ML for 1D (1st column), 2D (2nd column) and OBS. Rows are stratifi-
 746 cation, cross front velocity and cross front shear, respectively. The last row contains surface forcing used in 1D
 747 and 2D. Dashed lines separate the different stages 1–3 outlined in section 1. Specifically: a) 1D N^2 with PWP
 748 ML (grey dots), b) 2D N^2 with KPP boundary layer depth (grey dots), c) OBS N^2 with float depth (grey dots),
 749 d) 1D u^{xf} , e) 2D u^{xf} , f) OBS u , g) 1D u_z^{xf} , h) 2D u_z^{xf} , i) OBS u_z , j) Q_{NET} , k) τ^{af} (grey) and τ^{xf} (black), l) ML
 750 average viscosity ν .



751 FIG. 2. Vertical gradients predicted by 1D (purple) compared with those observed by the float (blue), Triaxus
 752 at 4 m (orange) and Triaxus at 12 m. Variables include (a) b , (b) T , and (c) S . Dashed lines separate the different
 753 stages 1–3 outlined in section 1.

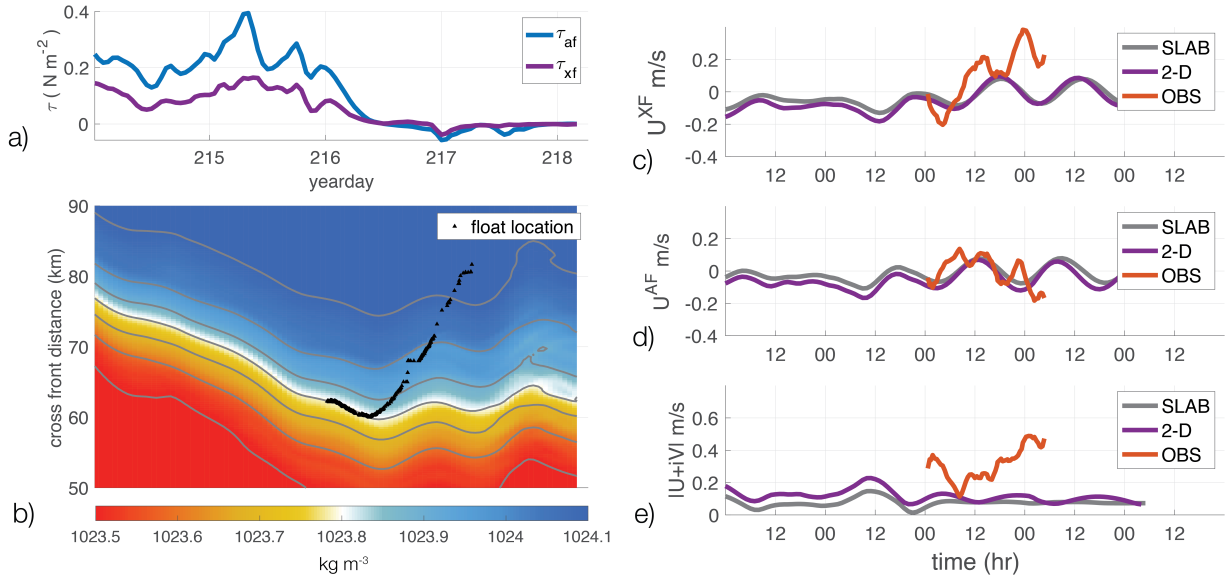
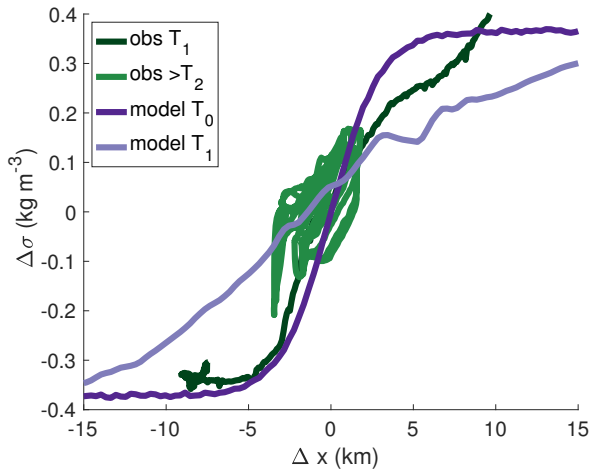
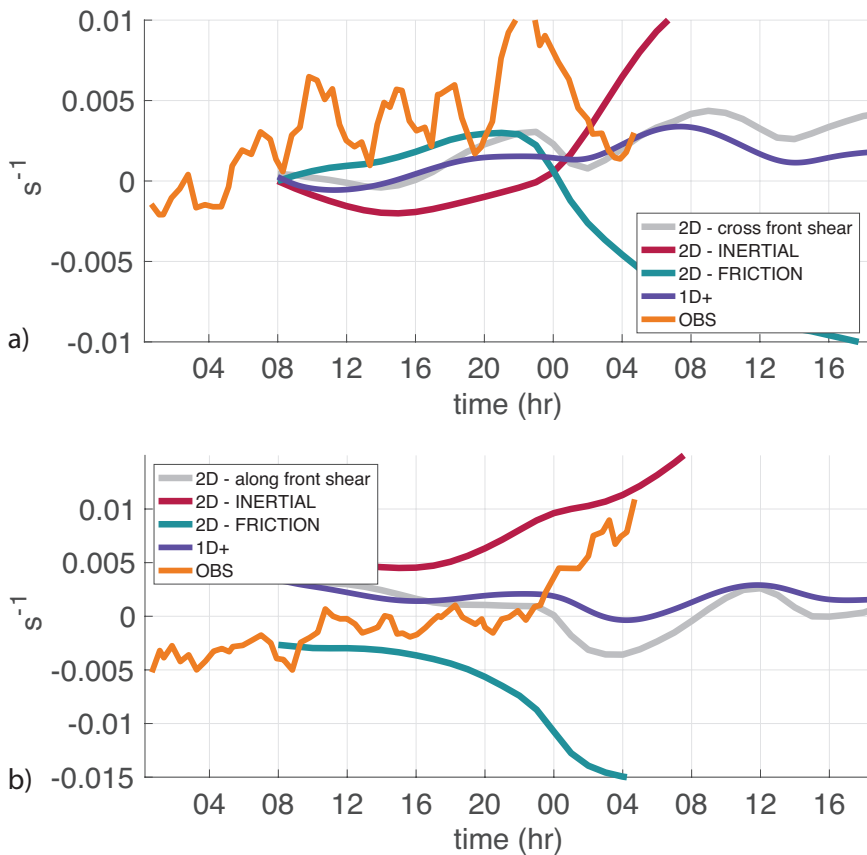


FIG. 3. NIO at the front as a response to a sudden decrease in winds. a) Wind stress starting 3 days after the start of 2D and 2 days before the survey began, τ^{af} is blue and τ^{xf} is purple. b) Plan view of surface ρ in 2D as a function of cross front distance and time. Grey lines are isopycnals, and black dots are the cross front distance of the float trajectory overlaid for reference. Surface velocity from 2D (purple), the solution to (6) and (7) (grey), and OBS (orange) for c) u^{xf} in models and u in OBS, d) u^{af} and -v in OBS and e) $|U|$ for model and OBS.



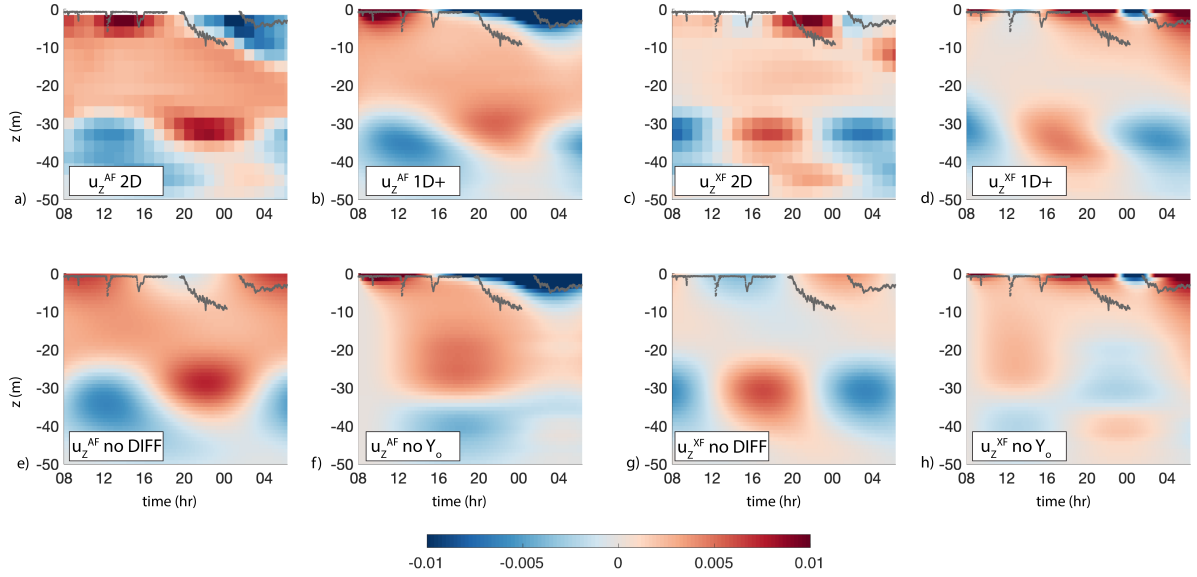
760 FIG. 4. Cross front density structure from OBS compared with 2D. The initial Triaxus transect (obs T_1 , dark
 761 green) crossed the entire front. Triaxus while following the float (obs $>T_2$, light green) surveyed the sharpest
 762 part of the front. 2D after one time step, 6 days before OBS (model T_0 , dark purple). Cross frontal structure in
 763 2D at the start of the Lagrangian survey (model T_1 , light purple) after 6 days of wind forcing.



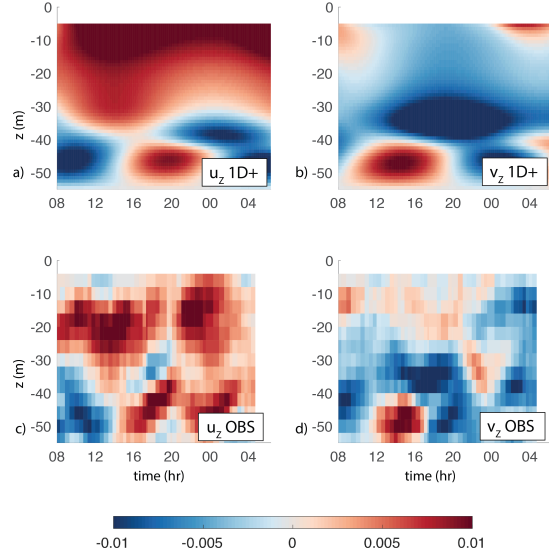
764 FIG. 5. (a) Cross front shear u_z^{xf} and (b) along front shear u_z^{af} . In 2D (grey), 1D+ (purple), and OBS (orange).

765 The contribution of the inertial terms, CORI + PRES (red) and friction, DIFF (teal) to the shear budget in 2D

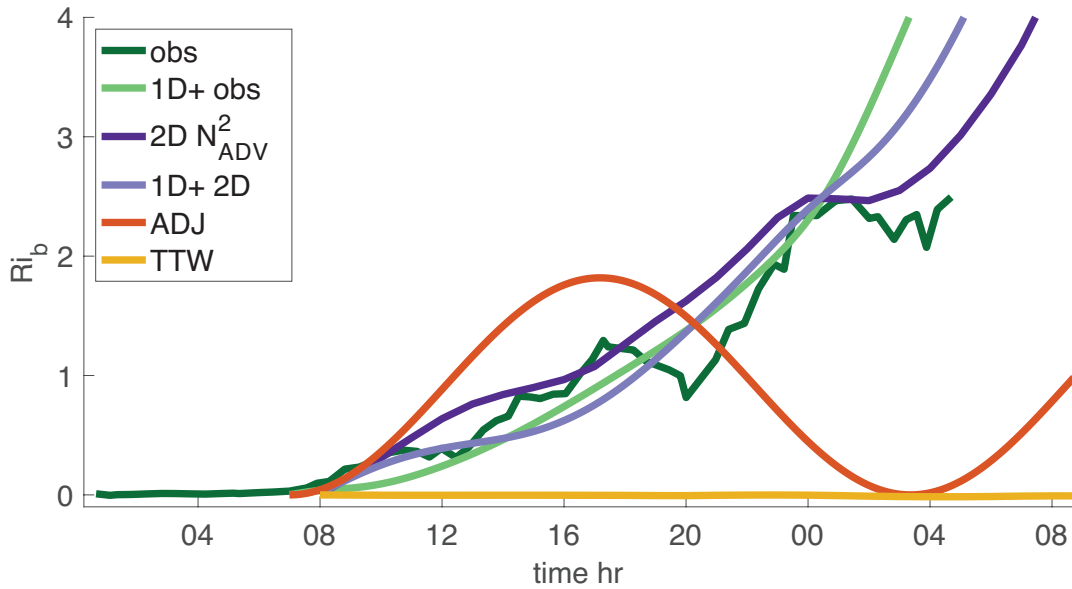
766 are also included.



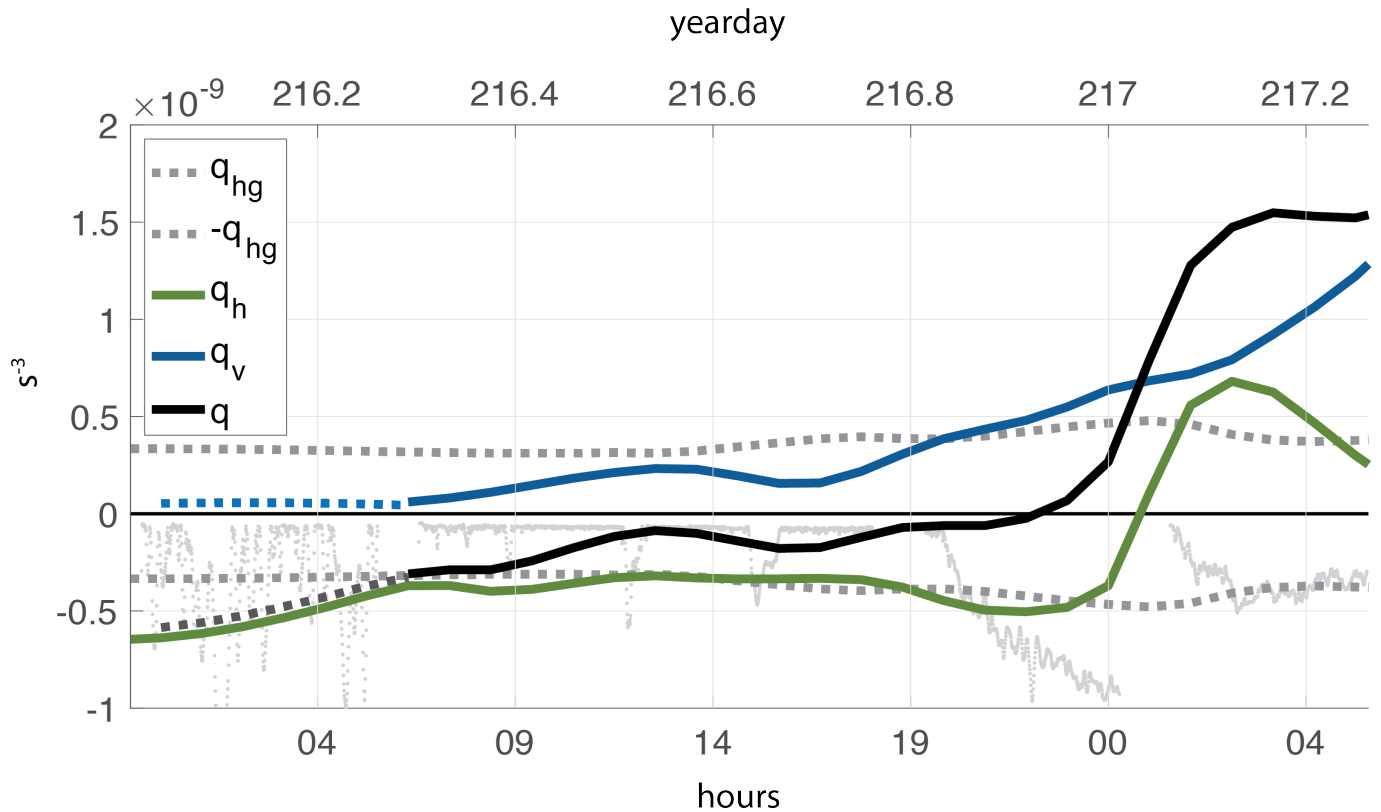
767 FIG. 6. Along front shear (AF - left panels) and cross front shear (CF - right panels) predicted by 2D (a, c),
768 1D+ (b, d), 1D+ without friction (e, g) and 1D+ without initial shear (f, h). Specifically: a) AF - 2D, b) AF -
769 1D+, c) XF - 2D, d) XF - 1D+, e) AF - 1D+ no DIFF, f) AF - 1D+ no Y_o , g) XF - 1D+ no DIFF, h) XF - 1D+ no
770 Y_o . Float depth from OBS (grey dots) are included for reference.



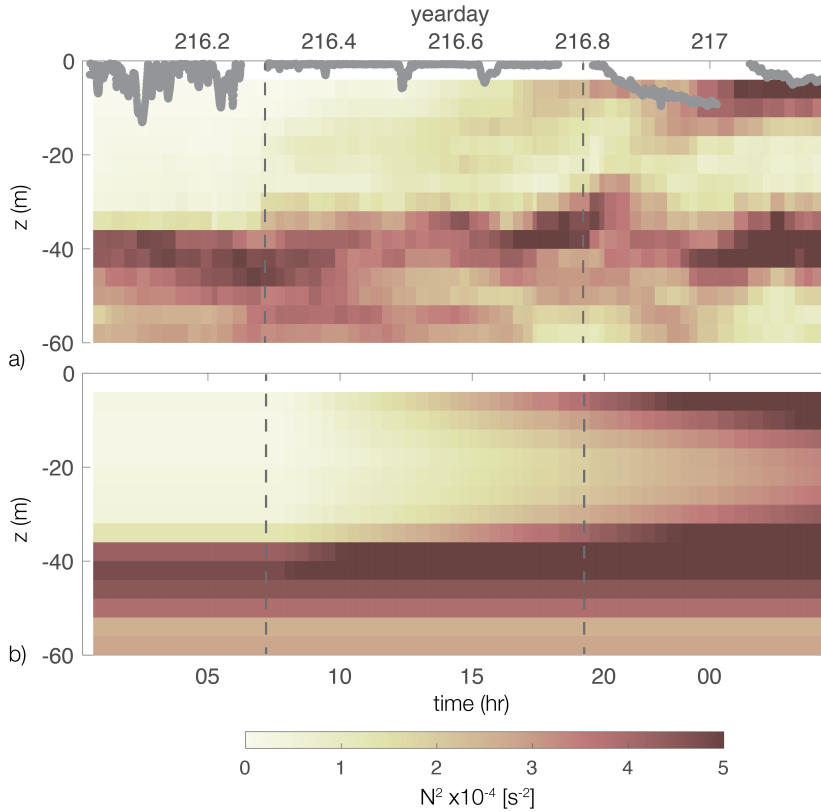
771 FIG. 7. Vertical shear predicted by 1D+ (initialized with OBS at the beginning of stage 2) compared with
 772 OBS. Only stage 2 and 3 are shown. a) 1D+ zonal shear, b) 1D+ meridional shear c) OBS zonal shear, d) OBS
 773 meridional shear.



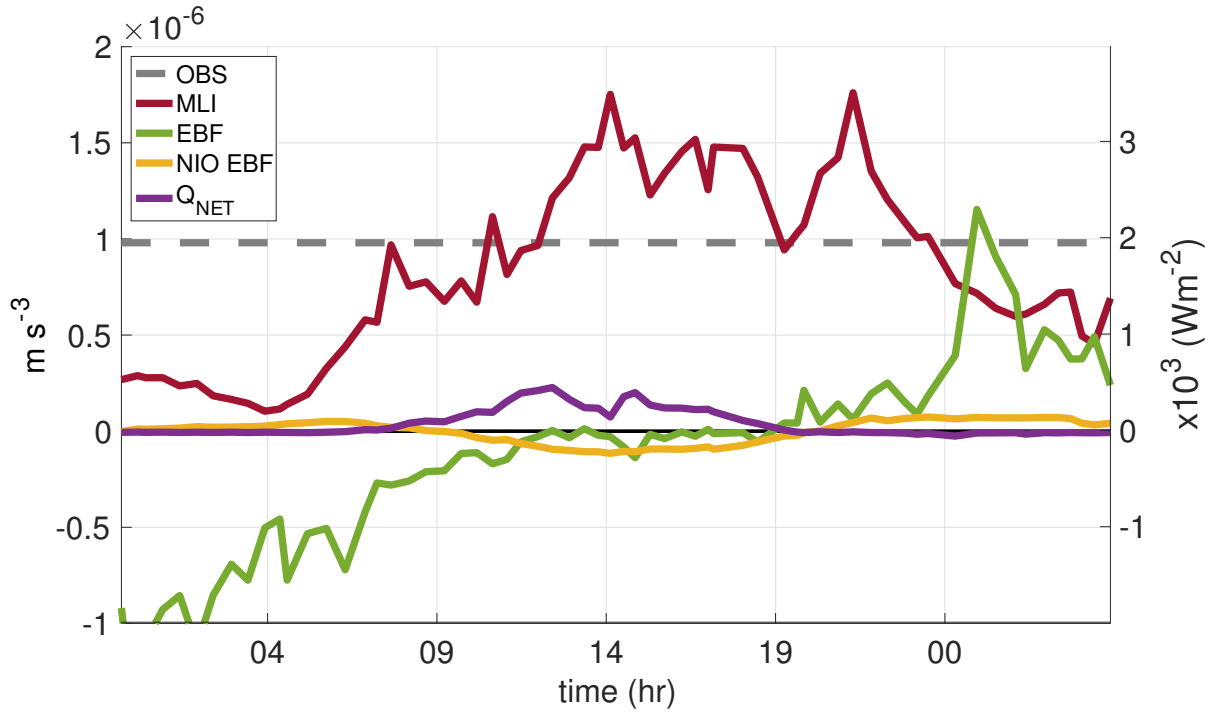
774 FIG. 8. N^2 (normalized to Ri_B) predicted by different models compared to the observations. N^2 from OBS
 775 and N^2_{ADV} for the 1D+ solution to OBS are in dark green and light green, respectively. N^2_{ADV} in 2D and the 1D+
 776 solution to 2D are in dark purple and light purple, respectively. Also included are N^2_{ADV} from 1D+ solutions to
 777 ADJ (TEND, ADV, PRES - orange) and TTW (ADV, PRES, DIFF - yellow).



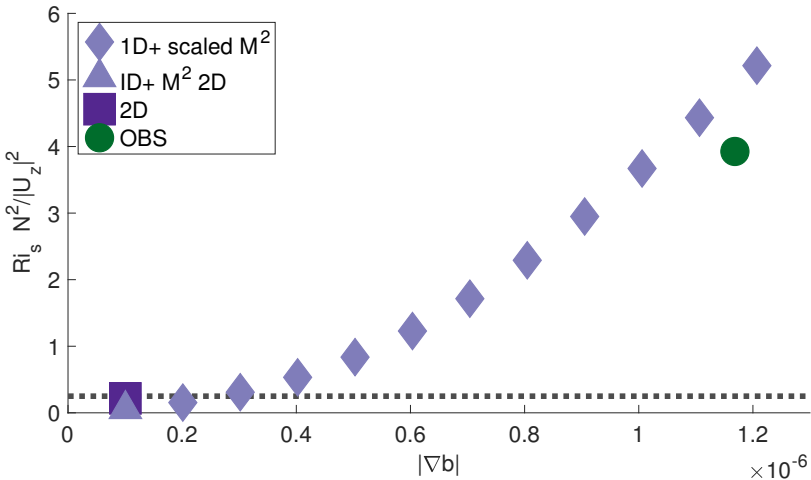
778 FIG. 9. PV at 8 m from 2D using N_{ADV}^2 to isolate changes resulting from vertical shear. Total q (black),
 779 horizontal q_h (green) and vertical q_v (blue). Grey dashed lines are the PV associated with thermal wind balance
 780 $q_{hg} = -b_{xf}^2/f$ (grey dashed lines). The observed float depth (scaled $\times 10^{-10}$) is included for reference.



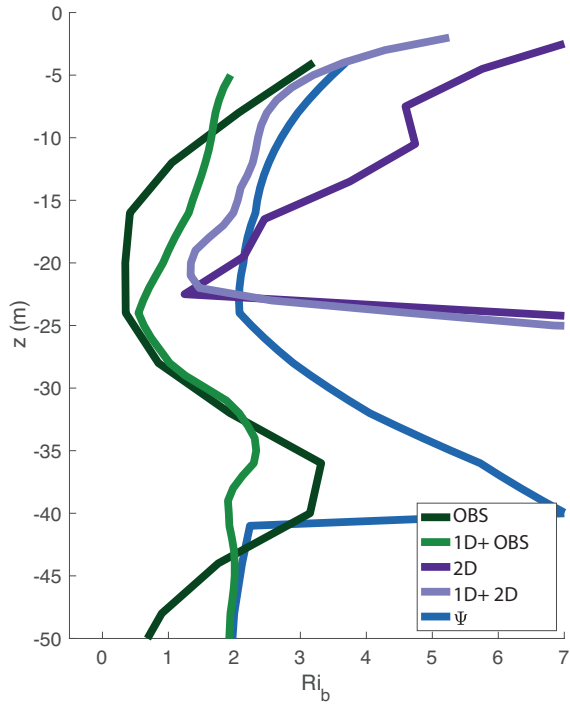
781 FIG. 10. Observed N^2 compared with that predicted by the MLE parameterization. a) N^2 from OBS in depth
 782 and time calculated from the Triaxus. Float position (grey dots) are included for reference. b) N^2 estimated from
 783 (14). Grey dashed lines represent the division between stages.



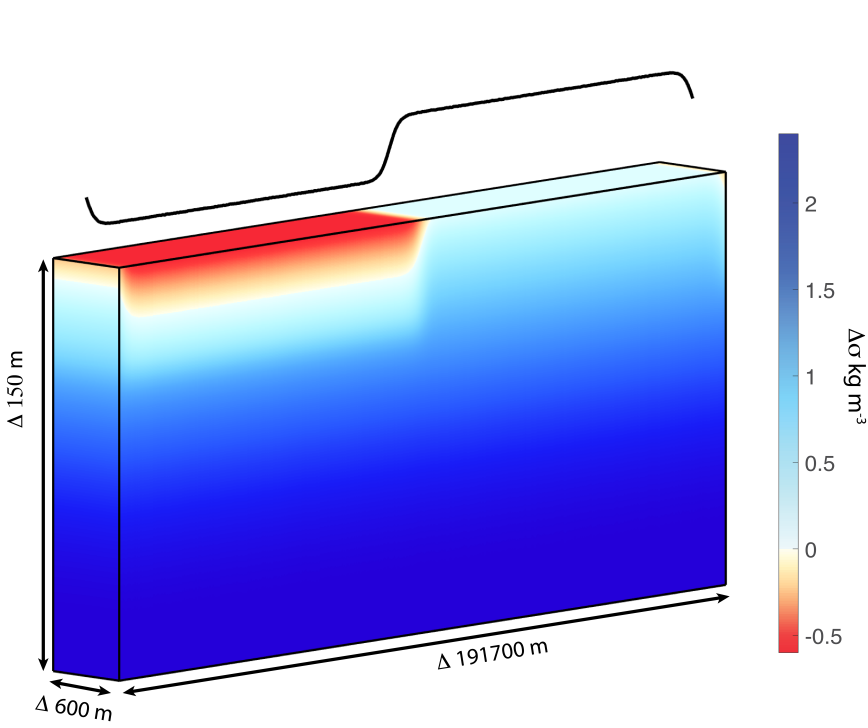
784 FIG. 11. Scalings of $w'b'$ (left axis) and effective Q_{NET} (right axis) for MLI (red), EBF (green), NIO EBF
 785 (yellow) and observed Q_{NET} (purple). Values were calculated as in Table 1 using observed ∇b_h , H , f , τ and
 786 solutions to (6) and (7). Average $w'b'$ derived from the observed N^2 is included for reference (grey dashed line).



787 FIG. 12. Comparison between shear Richardson number, Ri_s , and horizontal buoyancy gradient $|\nabla_h b|$. Ri_s was
 788 calculated during stage 3 (night-time mixing) from OBS (green), from 2D (dark purple) and from the solution
 789 to 1D+ for varying M^2 (light purple). The dashed grey line corresponds to critical $Ri_s = 0.25$.



790 FIG. 13. Vertical structure of N^2 in terms of Ri_b predicted by different models compared with observations
 791 (e.g. see Fig. 8 and Fig. 10). N^2 from OBS and N_{ADV}^2 from 1D+ initiated with OBS are in dark green and light
 792 green, respectively. N_{ADV}^2 from 2D and 1D+ initiated with 2D are in dark purple and light purple, respectively.
 793 N^2 predicted from MLI using (14) is in blue.



794 Fig. A1. Initial density structure in MITgcm. The along front distance is 600 m (2 grid points) with a cross
 795 front direction of 191700 m (639 grid points) and a horizontal resolution of 300 m. The vertical resolution was
 796 3 m extending to 150 m depth. The cross frontal density (scaled) is plotted above the front for visual reference.
 797 For an exact cross front density structure, see Fig. 4